

Structural Health Monitoring with Fiber Bragg Grating
Sensors Embedded into Metal Through Ultrasonic Additive
Manufacturing

A Thesis

Presented in Partial Fulfillment of the Requirements for the Degree
Master of Science in the Graduate School of The Ohio State
University

By

Sean Kelty Chilelli, B.S.

Graduate Program in Mechanical Engineering

The Ohio State University

2019

Master's Examination Committee:

Dr. Marcelo Dapino, Advisor

Dr. David Hoelzle

© Copyright by
Sean Kelty Chilelli
2019

Abstract

Structural health monitoring (SHM) is a rapidly growing field focused on detecting damage in complex systems before catastrophic failure occurs. SHM systems provide the potential to improve safety and significantly reduced costs. Advanced sensor technologies are necessary to fully harness SHM in applications involving harsh or remote environments, life-critical systems, mass production vehicles, robotic systems, and others. Fiber Bragg grating (FBG) sensors are an attractive solution for in-situ health monitoring due to their low weight, resistance to electromagnetic noise, ability to be multiplexed, and accuracy for real-time measurements. However, effective embedment of FBG sensors into metal has proved challenging. Ultrasonic additive manufacturing (UAM) has been demonstrated for solid-state fabrication of 3D structures with embedded FBG sensors. In this thesis, UAM embedded FBG sensors for SHM applications are investigated. Embedment of a fiber using UAM was shown to have little effect on the tensile and fatigue properties of aluminum coupons. Furthermore, the ability of UAM embedded FBG sensors to detect and monitor crack growth in Compact Tension (CT) specimens is demonstrated. UAM embedded FBG sensors 3 mm from the initiation site were able to accurately detect cracks of length 0.286 ± 0.033 mm. UAM embedded FBG sensors are shown to accurately track crack growth until near failure. Furthermore, UAM embedded FBG sensors 3 mm, 6 mm, and 9 mm from the initiation site detected a crack that initiated to 0.350 mm. Finally,

the potential for high temperature applications is also examined through elevated temperature testing. Fiber optics embedded into aluminum using UAM are shown to be more resilient to degradation at elevated temperatures than exposed fibers. UAM embedded FBG sensors are therefore shown to be an effective type of sensor for SHM applications.

To Julie, Ellen and Tony

Acknowledgments

I must primarily thank my advisor, Professor Marcelo Dapino, for giving me the opportunity to join the Smart Materials and Structures Laboratory. His insight and support from the very beginning has been invaluable and has allowed this project to flourish. His guidance was crucial in my own growth as an engineer and as a researcher. I would also like to thank Professor David Hoelzle for his teaching and for sitting on my committee.

I would like to express my gratitude to Tom Greetham at Moog, Inc. for providing direction and technical support. It was always a pleasure to update him on the project and discuss future research paths. Thanks also for the technical support of Paul Guerrier and George Small of Moog, Inc. and Paul Deadman, Charles England, and Andy Strohacker of Moog, Inc (Insensys Ltd.). Thank you to Jack Schomer, who provided valuable guidance as I took the reigns on this project from him. My gratitude goes out to Dr. Ziran Wu for his assistance. Thank you to Bryant Gingerich, for always being there to answer my questions and concerns. In addition, I would like to thank all my colleagues in the Smart Materials and Structures Lab, especially Han Tiangyan, Hongqi Guo, Yongson Rong, Gowtham Venkatraman, Leon Headings, Tommie Blackledge, and Jennifer Morris.

I would also like to acknowledge the funding support of the National Science Foundation Industry-University Cooperative Research Center on Smart Vehicle Concepts (www.SmartVehicleCenter.org) established under grant IIP-1238286 and grant IIP-1738723.

Thank you to all of my friends who made this journey possible. Thank you to my growing family, my mother-in-law Lois, as well as Sammy, Molly, Ginny, Joe, and Marie. Thank you to Jeffery Chang, whose friendship and support are inspiring. His impact on my life can't be understated, this wouldn't have been possible without him. I must express my profound gratitude to my wife and best friend, Julie Rolla, whose continual and unquestioning support – combined with a one of a kind passion for adventure – makes everyday possible. I could not have come this far without the support of my parents, Ellen and Tony, nor my siblings, Patrick, Brendan and Leanna. Thank you all for shaping me into the person I am today.

Vita

July 15, 1993 Born - Denver, Colorado

May 2011 International Baccalaureate Diploma,
George Washington High School

August 2015 B.S. Mechanical Engineering and
Materials Science & Engineering,
University of California, Berkeley

August 2015 - August 2017 Mechanical Engineer, Doblet Inc.

August 2017-August 2019 Graduate Research Associate,
The Ohio State University.

Publications

Research Publications

S.K. Chilelli, M.J. Dapino, J.J. Schomer, “Detection of crack initiation and growth using fiber Bragg grating sensors embedded into metal through ultrasonic additive manufacturing,” *Sensors*. To Be Submitted.

Z. Wu, M.J. Dapino, S.K. Chilelli, “Convolutional neural network for metallic fracture detection using digital image correlation,” *Sensors*. To Be Submitted.

Fields of Study

Major Field: Mechanical Engineering

Studies in Smart Materials and Structures: Dr. Marcelo Dapino

Table of Contents

	Page
Abstract	ii
Dedication	iv
Acknowledgments	v
Vita	vii
List of Tables	x
List of Figures	xi
1. Introduction	1
1.1 Structural Health Monitoring	1
1.2 Fiber Bragg Grating Sensors	5
1.3 Ultrasonic Additive Manufacturing	11
1.3.1 Dissimilar Material Joining in UAM	14
1.4 Method of Embedding Sensors through UAM	15
1.4.1 Laser Pointer Demonstrator	18
1.5 Experimental Test Equipment	20
1.6 Problem Statement	24
1.6.1 Thesis Outline	24
2. Mechanical Properties of Metal with Embedded FBG Sensor	26
2.1 Tensile Properties	26
2.1.1 Experimental Methods	26
2.1.2 Results and Discussion	27
2.2 Fatigue Properties	30
2.2.1 Experimental Methods	31

2.2.2	Results and Discussion	31
3.	Crack Propagation Detection and Prognostic Analysis	33
3.1	Crack Propagation Tracking and Early Crack Detection	33
3.1.1	Experimental Methods	33
3.1.2	Results and Discussion	36
3.2	Prognostic Analysis	44
3.2.1	Experimental Methods	44
3.2.2	Results and Discussion	47
3.3	Verification of Strain in CT Coupons	53
4.	Elevated Temperature Characterization	58
4.1	Static Temperature Testing of Embedded Fiber Optic Cable	58
4.1.1	Experimental Methods	59
4.1.2	Results and Discussion	59
4.2	Variable Temperature Testing With Embedded FBG	62
4.2.1	Experimental Methods	62
4.2.2	Results and Discussion	64
5.	Conclusions and Future Prospects	67
	Appendices	70
A.	Coupon Geometries	70
B.	Additional Results and Considerations	71
B.1	Sensor Embedment Process	71
B.2	Fatigue Testing	71
B.3	Crack Growth	71
B.4	Elevated Temperature	78
	Bibliography	80

List of Tables

Table	Page
1.1 Summary of common aircraft maintenance checks [8]. Values are approximate and may vary with different manufacturers.	4
2.1 Summary of tensile test results.	28
3.1 Length of crack in CT specimen at earliest detection using a UAM embedded FBG sensor 3 mm from notch. Ranges are due to crack entering a DIC speckle and consequently being unable to optically determine a precise endpoint.	42
3.2 Comparison of early through crack length detection of UAM embedded FBG sensor to common aerospace NDI techniques [60].	43
4.1 Summary of initial tests performed at elevated temperatures.	60

List of Figures

Figure	Page
1.1 The different levels of sophistication possible in health monitoring applications [4].	3
1.2 Schematic of Bragg diffraction [19].	6
1.3 9 kW Fabrisonic SonicLayer 4000 UAM system.	11
1.4 Welding assembly of a 9 kW Fabrisonic SonicLayer 4000 UAM system [33].	12
1.5 The bilayer configuration used for Al/Ti welding processes [35]. . . .	15
1.6 Successful UAM weld of a Al/Ti bilayer onto a block of Ti-6Al-5V made through powder bed fusion.	16
1.7 The basic procedure for embedding sensors into metal through UAM.	17
1.8 Cross section of a drawing of an optical fiber compared to a backlit cross section of a UAM embedded optical fiber [33].	18
1.9 The lens and fiber have been installed into the channels of the UAM structure. Note the rough surface texture around the embedded sensor which is imparted by the UAM process after welding each layer. This texture can be easily machined away.	19
1.10 The welds over the lens and fiber show no tearing in foil and complete encapsulation. A smooth texture occurs above channels since no welding is occurring at those locations.	19
1.11 Different angles demonstrating the completed and fully functional laser pointer demonstrator.	20

1.12	A strain field during the cyclic loading of a CT specimen generated through DIC.	21
1.13	Connection diagram of the various equipment, software and signals used in this thesis. Analog signals are shown with a solid red line and digital signals are shown with a green dotted line. Not all experiments performed used every piece of the equipment shown.	23
2.1	Cross sections of the four coupon geometries that underwent tensile testing: (a) bulk Al 6061-T6, (b) UAM control, (c) empty channel, (d) embedded fiber. Al 6061 is shown in grey, UAM layers are shown in blue, the channel is shown in black, and optical fiber is shown in red.	27
2.2	Tensile testing results from all samples.	29
2.3	Finite element analysis of tensile testing with and without an embedded fiber.	30
2.4	Results from fatigue testing. Literature values from MMPDS [54]. All UAM samples contain an embedded fiber.	32
3.1	Experimental setup showing a CT coupon installed in the load frame.	35
3.2	Compact tension (CT) specimen with one embedded FBG sensors built using UAM used in crack initiation and strain tracking testing. A fine speckle has been applied for DIC tracking.	37
3.3	The raw FBG strain signal throughout the life of a CT specimen. The end of the pre-cracking phase is denoted by the red arrow. The vertical lines at toward the end of the sampling are likely artifacts of the FBG fiber slipping as the crack neared the embedded fiber.	38
3.4	Peak reflected wavelength from FBG during the pre-cracking phase, extracted from Figure 3.3. The red box shows the range of Figure 3.5.	38
3.5	Detailed view of the red box in Figure 3.4, showing the strain over about ten cycles. Note the two lower cycles used to trigger the DIC.	39
3.6	Detailed view of the green box in Figure 3.5, showing the maximum values of a set of 8 cycles. The peaks are marked with a triangle.	39

3.7	The peaks of the FBG strain signal during the pre-cracking phase. After every eight cycles, the DIC was triggered with a low peak (not shown). The red box shows the boundaries of Figure 3.8.	40
3.8	Detailed view extracted from red box in Figure 3.7 of peaks of the FBG strain signal during the pre-cracking phase are shown for four sets of eight cycles, The green x markers indicate the mean of each set. . . .	41
3.9	Vertical strain measurements from a FBG sensors embedded into a CT specimen through UAM and the average strain from DIC in the region of the FBG; (a) from the end of the pre-cracking phase (\sim cycle 2 000) to sample failure (\sim cycle 10 500); (b) detailed view of (a) approximately from cycle 3 000 to 8 500.	44
3.10	Comparison of the FBG strain signal and the average peak strain from DIC in the region of the FBG after (a) 2 000, (b) 4 000, (c) 6 000, (d) 8 000 and (e) 10 000 cycles.	45
3.11	The FBG strain signal and the average peak strain from DIC in the region of the FBG as the crack length increased.	45
3.12	Compact tension (CT) specimen with three embedded FBG sensors built using UAM used in prognostic testing.	46
3.13	The load frame displacement (a) and the FBG signals from sensors embedded 9 mm (b), 6 mm (c) and 3 mm (d) from the notch over the entire prognostic analysis test.	48
3.14	Detailed view of Figure 3.13 between cycles 749 to 761. Shown is the load frame displacement (a) and the FBG signals from sensors embedded 9 mm (b), 6 mm (c) and 3 mm (d) from the notch. Note the alternating crack growth phases with high strain and low amplitude phase with lower strain. The number of cycles of the crack growth phase was reduced toward the end of the test to ensure enough data was obtained as the crack grew.	49
3.15	Crack detection analysis during low amplitude cyclic loading for embedded FBG 3 mm from notch tip. For this an subsequent images, the dashed line represents three standard deviations above the normal set mean.	50

3.16	Crack detection analysis during low amplitude cyclic loading for embedded FBG 6 mm from notch tip.	50
3.17	Crack detection analysis during low amplitude cyclic loading for embedded FBG 9 mm from notch tip.	51
3.18	Crack detection analysis during high amplitude cyclic loading for embedded FBG 3 mm from notch tip.	51
3.19	Crack detection analysis during high amplitude cyclic loading for embedded FBG 6 mm from notch tip.	52
3.20	Crack detection analysis during high amplitude cyclic loading for embedded FBG 9 mm from notch tip.	52
3.21	DIC of CT coupon with a load of 2000 N. Units of the legend are $\mu\epsilon$. The locations of embedded fibers at 3 mm, 6 mm and 9 mm are labeled.	54
3.22	Location of loading and boundary conditions for FEA analysis.	56
3.23	Results of Abaqus FEA analysis of CT specimen with (a) no crack, (b) a 0.35 mm crack, and (c) a 1.5 mm crack.	57
4.1	Cross section of coupon showing fiber degradation. Note the lack of clear internal fiber components.	61
4.2	Picture of coupons from Test 6 showing bubble formation.	61
4.3	Example results from Test 7 showing (a) an intact coupon without any bubbles and (b) a cross section showing a fully intact fibers coating and structure.	62
4.4	Elevated temperature coupons built using UAM with high temperature strain gauges affixed to the outside. FBG fibers are embedded down the length of each coupon.	63
4.5	Elevated temperature testing of two UAM embedded FBG sensors. The strain measurements of two coupons with embedded FBG sensors and strain gauges is shown using the right axis. Using the left axis and shown in black is the temperature measurement from a thermocouple.	64

4.6	Elevated temperature cyclic testing of one UAM embedded FBG sensors. The FBG signal was measured during a cyclic temperature test with increasing oven set points. Once noticeable deviation occurred at 350°C, the test was performed one more time to see if permanent damage had occurred.	65
4.7	Comparison of the cross section of a UAM embedded FBG that has not undergone any thermal loading (a), to the cross section of the embedded FBG from the cyclic testing (b).	66
A.1	Drawing of coupon used in the tensile testing and elevated temperature testing. Dimensions in mm. Based on designs from ASTM E8 [53]. .	70
A.2	Compact tension (CT) specimen geometry used in crack detection. All dimensions are in mm. Based on designs from ASTM E647 [58]. . . .	70
B.1	After one layer welded by UAM, three channels are machined.	72
B.2	The FBG sensors are then carefully placed in the channels.	72
B.3	Additional layers are then welded with UAM over the FBG sensors. .	73
B.4	A CNC machine mills out the final coupon geometry.	73
B.5	Initial fatigue coupons failed outside the gauge region due to the fibers exiting coupons outside the grip region.	74
B.6	DIC produced strain fields during the growth of a crack.	74
B.7	To compare the FBG signal to the DIC strain, the DIC strain was averaged in the region of the fiber. The fiber is embedded at the white dotted line. The area of the strain field averaged in shown in the red box.	75
B.8	The ratio between the voltage signal from the digital to analog converter and the DIC mean strain in the fiber region was found. The early region, shown in orange, was averaged and used to convert the FBG voltage signal to strain.	76

B.9	The CT specimen at cycle 195 when the statistical analysis of the FBG signal first determined the presence of a crack.	76
B.10	Detailed view of Figure B.9. The red arrow shows the location and length of the crack. Note how the crack enters a speckle, so the exact end point cannot be determined. Each pixel of the photograph corresponds to 0.0054 mm.	77
B.11	Additional cross-sections of coupons that have undergone elevated temperature testing; (a) control with no elevated temperature testing; (b) coupons tested at 350°C for 20 minutes; (c) coupons tested at 400°C for 20 minutes. Note that both (a) and (b) show no damage to fiber structure (cracks in (b) are likely due to insufficient channel depth). On the other hand, (c) shows cross-sections with clearly damaged fibers and signs of remelting of the acrylate.	78
B.12	Example of smoke stains at the fiber exit point of the coupon.	79

Chapter 1: Introduction

1.1 Structural Health Monitoring

Structural health monitoring (SHM) is the process of using sensors to detect damage in systems before catastrophic failure occurs. The basic procedure of SHM begins with usage monitoring, where sensors measure damage-sensitive features during normal operation before any damage is present. By continuing to measure these features throughout the life of the structure, statistical analysis can be used to identify the onset of damage. Beyond the mere identification of damage, advanced SHM systems aim to predict the level of damage present and then estimate the remaining lifetime of the system.

Damage can be defined as defects introduced into a system that adversely effects its current or future performance [1]. The size of the damage, the time scale of damage accumulation, and the effect of the damage on the entire system can vary greatly, which creates a difficult engineering challenge in many SHM applications. In addition, many external factors such as temperature, humidity, wind, and discrete abnormal loading events, may create unexpected sensor responses [1]. Therefore, to correctly identify damage it is necessary to have robust, carefully located, sensor networks combined with extensive knowledge of the environment and loading conditions.

The development and application of SHM are pursued due to their potential to improve safety and significantly reduced costs. Historically, damage identification has always been an important aspect of engineering, with the first development of standardized evaluation techniques occurring during the industrial revolution [2]. The majority of SHM research has taken place since the 1970s, coinciding with the development of improved sensors and computation abilities that made SHM possible [3]. SHM systems can be broadly categorized into five main groupings as shown in Figure 1.1. In general, most non-destructive inspection (NDI) techniques are only able to detect local damage and can thus be classified with sophistication of Level I or II [4]. Sensor systems are able to have increasing levels of sophistication ranging from Level II to Level V based on complexity. SHM systems with higher levels of sophistication provide increased benefits over simpler systems and therefore research into these sophisticated systems is actively being pursued.

SHM applications are becoming increasingly more common in many civil engineering structures; however, a number of industries, especially the aerospace and automotive industries, require improved sensors, system monitoring, and diagnostic tools. Properly implemented SHM will reduce the need for NDI which typically requires the system to be out of commission as costly, labor intensive testing is performed [4]. Furthermore, when NDI is relied upon, any structure that develops defects or cracks during normal operation is allowed to continue until the next inspection. This has resulted in many catastrophic failures when defects were not present during the last inspection. Often aircraft or parts are retired based solely on the number of operating hours, a criteria that can both drastically under or overestimate the actual health of the structure [5]. For example, a common significant scheduled maintenance

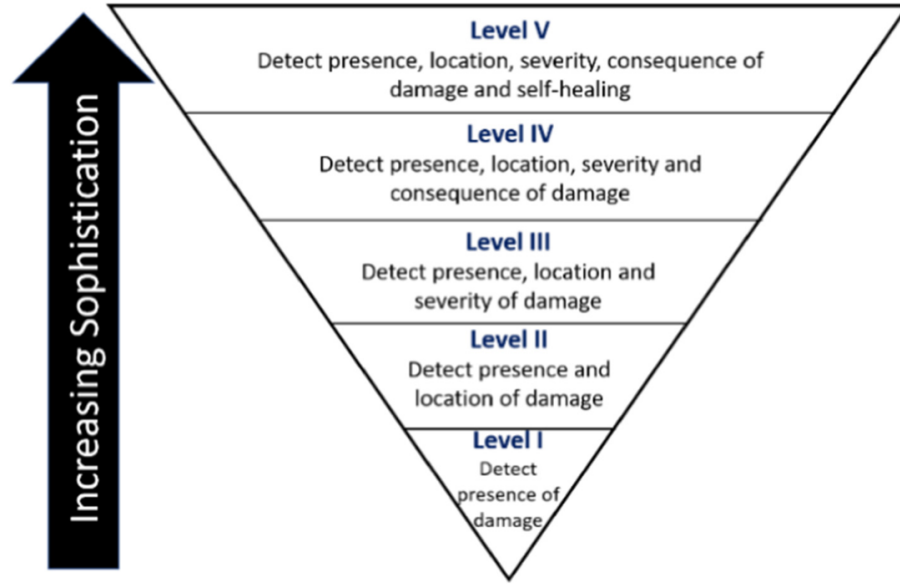


Figure 1.1: The different levels of sophistication possible in health monitoring applications [4].

of the Boeing 737NG, the C-Check, is performed every 2800 flight cycles, regardless of actual damage [6]. Other example maintenance checks are summarized in Table 1.1. In practice, there are many other factors which determine the actual health of the aircraft including environment, style, discrete events and minute material differences. SHM systems could allow continuous and safer operations where defects are detected in real time, thus generating significant cost savings with improved safety [7]. Creating safer systems where damage is detected early on is especially important in the future of the aerospace industry.

Significant research has examined the potential cost savings of SHM systems in the aerospace industry. For example, over 27% of the total vehicle life cycle cost comes from inspection and maintenance [9]. Further, nearly 80% of maintenance

Table 1.1: Summary of common aircraft maintenance checks [8]. Values are approximate and may vary with different manufacturers.

Name	Frequency	Downtime	Description
A-Check	Every two months	Overnight	All technical systems
B-Check	Every 6 Months	Three days	Technical systems in detail
C-Check	Every two years	Two weeks	Structures and systems
IL-Check	Every four years	Three weeks	Structural and corrosion
D-Check	Every ten years	2 Months	Complete inspection and overhaul

departure delays could be prevented with SHM sensors [8]. SHM could be implemented to drastically reduce these costs.

There are four main aspects that are often used to describe the SHM process: (1) operational evaluation, (2) data acquisition, (3) feature extraction, and (4) model development [1, 3]. Operational evaluation examines the system to understand the possible damage features. Data acquisition focuses on the types of sensors, number of sensors, locations of sensors, and any additional data recording hardware and software. Feature extraction describes the process of identifying variables that are sensitive to damage and using those variables to detect the presence of damage. The fourth and most advanced process is that of model development, where analysis is performed to determine the location, type and severity of the damage and to determine the useful remaining life of the structure. Recent developments in the field include using artificial intelligence, including neural networks, for prognostic analysis in SHM applications [10]. While each of these processes is somewhat application dependent, operational evaluation and model development are particularly so. Consequently, this thesis mostly focuses on data acquisition and feature extraction.

One of the most crucial factors in effective SHM applications is the choice of sensor. Many types of sensors can be used and often more than one type is used at a time. Some examples include strain gauges, various fiber optic sensors, thermocouples, piezoelectric sensors, electrochemical sensors, wireless sensors, optical cameras, acoustic detection, smart coatings, ultrasonic sensors, and accelerometers, [4, 5, 11, 12]. Continued research into SHM sensors is critical, as without improved sensor technologies, SHM may not become a practical and cost-effective for new industries to adopt [6].

1.2 Fiber Bragg Grating Sensors

The sensor networks used in SHM should be minimally invasive and have a long life in order to accurately detect damage in real time over the life of the system [11]. Fiber Bragg grating (FBG) strain sensors are one potential SHM sensor already used in many structural applications including building foundations [13], wind turbines [14], composite cure monitoring [15], bridges [16], concrete infrastructure [4], and many other applications [17].

FBG Theory

There are a few important principles crucial to understanding the function of FBG sensors. Bragg diffraction is the constructive interference of reflected waves at specific incident angles on a crystal lattice and was first discovered in 1913 earning William Henry Bragg and his son, William Lawrence Bragg, the Nobel Prize [18]. The basic principle of Bragg diffraction is that each layer of a periodic lattice reflects incident waves, which at specific incident angles cause constructive interference of the reflected light leading to a resonant wavelength. When this specific condition occurs, the waves

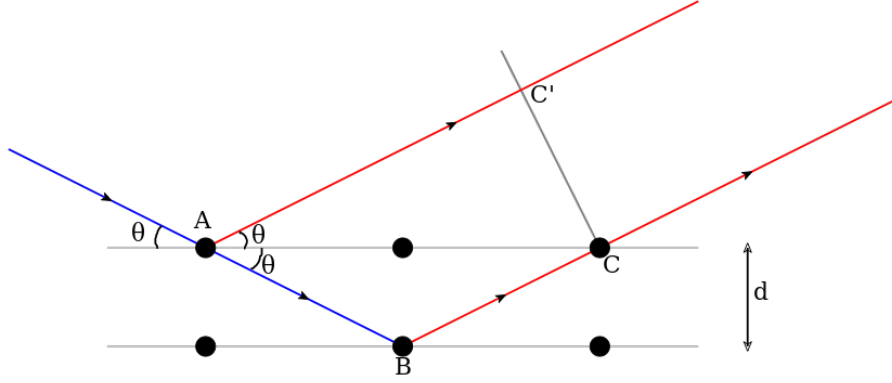


Figure 1.2: Schematic of Bragg diffraction [19].

constructively interfere producing a strong reflected wavelength. The principle can be derived through the following procedure.

Examining Figure 1.2, an incident wave shown in blue strikes a lattice at point A with a periodic spacing of d at an angle of θ . At that instance, some of the energy of the wave is transmitted and some is reflected. The transmitted wave then strikes the second layer at point B and again the wave is transmitted and reflected. If each of the reflected waves has the same phase by the point C and C' then they will constructively interfere [18]. In other words, if the difference in path length is equal to an integer value of the wavelength, constructive interference will occur. This geometric condition can be summarized by

$$(AB + BC) - (AC') = n\lambda. \quad (1.1)$$

Because the lattice is periodic, when Equation 1.1 is satisfied for one layer, it is satisfied for all layers, producing a strong reflected intensity. Using basic trigonometry, the distances defined above can be defined based on d , θ and λ ,

$$AB = BC = \frac{d}{\sin \theta}, \quad (1.2)$$

$$AC = \frac{2d}{\tan \theta}, \quad (1.3)$$

then,

$$AC' = AC \cos \theta = \frac{2d}{\sin \theta} \cos \theta^2. \quad (1.4)$$

Therefore, the Bragg condition can be rewritten as:

$$\left(\frac{d}{\sin \theta} + \frac{d}{\sin \theta} \right) - \frac{2d}{\sin \theta} \cos \theta^2 = n\lambda, \quad (1.5)$$

which reduces to

$$\frac{2d}{\sin \theta} - \frac{2d}{\sin \theta} \cos \theta^2 = n\lambda, \quad (1.6)$$

$$\frac{2d}{\sin \theta} (1 - \cos \theta^2) = n\lambda, \quad (1.7)$$

$$\frac{2d}{\sin \theta} (\sin \theta^2) = n\lambda, \quad (1.8)$$

$$2d \sin \theta = n\lambda. \quad (1.9)$$

Finally, if the wave is traveling in a medium (and not a vacuum), the index of refraction n_{eff} of the medium must be included

$$2dn_{eff} \sin \theta = n\lambda. \quad (1.10)$$

This result paved the way for characterization in materials science and allowed for a deeper understanding of crystalline structures.

The second principle behind FBG sensors is that of the Fresnel effect, which describes the phenomenon that when light is incident on the interface of two optical media, some light is transmitted and some is reflected [18].

FBG sensors are the result of the combination of Bragg diffraction and the Fresnel effect in a fiber optic cable. Periodic layers of a different refractive index are introduced into a fiber optic cable, typically through UV etching. When light is transmitted down the fiber, some light is reflected back due to the Fresnel effect each time the wave hits one of the periodic gratings. If the Bragg condition is satisfied, those reflected wavelengths constructively interfere, resulting in a specific wavelength that is reflected back at high intensity [20]. The Bragg condition defined above can be modified for the FBG case by changing d (the lattice spacing) to Λ (the grating spacing), setting n equal to 1 (for the lowest order Bragg resonance), and noting that θ is equal to 90 degrees (and therefore $\sin \theta = 1$) [21]:

$$\lambda = 2\Lambda n_{eff}. \quad (1.11)$$

FBG sensors are typically implemented with the transmitted light having a wide range of wavelengths. The FBG sensors used in this thesis had nominal reflected wavelengths of about 1550 nm. Since the refractive index of the fiber core (silica) is about 1.5, we can estimate (from Equation 1.11) the grating spacing to be about 516.67 nm [22]. Manufacturers are able to change the nominal spacing of the grating to create different reflected peaks at various points in the same fiber (called multiplexing).

The strain sensing aspect of FBG sensors comes from the fact that when the fiber itself is strained, the spacing of the grating changes, which in turn leads to the peak reflected wavelength changing [18, 23]. Due to the photo-elastic phenomenon, the index of refraction of a material may change when the material is strained. This is a unitless ($[\frac{\Delta n}{\varepsilon}]$) material property, defined by the photo-elastic coefficient, ρ_e , which is reported as around 0.22 for fiber optic silica cores [22]. We can take the partial derivative of the Bragg condition with respect to strain (ε) to determine the relationship between strain and shift in wavelength, noting the chain rule must be used as both Λ and n_{eff} are dependent on displacement,

$$\frac{\Delta \lambda}{\varepsilon} = 2n_{eff} \frac{\delta \Lambda}{\delta \varepsilon} + 2\Lambda \frac{\delta n_{eff}}{\delta \varepsilon}. \quad (1.12)$$

Substituting from the Bragg condition, $2\Lambda = \frac{\lambda}{n_{eff}}$ and $2n_{eff} = \frac{\lambda}{\Lambda}$, Equation 1.12:

$$\frac{\Delta \lambda}{\varepsilon} = \frac{\lambda}{\Lambda} \frac{\delta \Lambda}{\delta \varepsilon} + \frac{\lambda}{n_{eff}} \frac{\delta n_{eff}}{\delta \varepsilon}, \quad (1.13)$$

$$\frac{\Delta \lambda}{\varepsilon} \frac{1}{\lambda} = \frac{1}{\Lambda} \frac{\delta \Lambda}{\delta \varepsilon} + \frac{1}{n_{eff}} \frac{\delta n_{eff}}{\delta \varepsilon}. \quad (1.14)$$

Noting that the first term on the right hand side of Equation 1.14 is equal to one as the strain experienced by the fiber will match the strain of the grating itself. The second term is the change in refractive index with strain, which has already been defined as the photo-elastic coefficient. Convention in the definition of the photo-elastic coefficient is that this term is negative because the index of refraction decreases when the material is positively strained,

$$\frac{\Delta \lambda}{\varepsilon} \frac{1}{\lambda} = 1 - \rho_e, \quad (1.15)$$

$$\frac{\Delta \lambda}{\lambda} = (1 - \rho_e)\varepsilon, \quad (1.16)$$

which gives a relationship between wavelength shift and strain,

$$\varepsilon = \frac{\Delta\lambda}{\lambda(1 - \rho_e)}. \quad (1.17)$$

Note that in applications with varying temperatures, an additional term is required to account for thermo-optic effects [18].

FBG in SHM applications

There are a number of benefits to FBG sensors that make them attractive for SHM. FBG sensors are immune to electromagnetic interference, can be multiplexed, are low cost, require no additional wiring, have high strain resolution, resist corrosion, and are lightweight with a minimally invasive geometry [13]. FBG sensors can provide structural loading data by ensuring strong coupling between the structural matrix and the sensor [24]. Although this coupling has been achieved in many laminate polymer applications through direct embedment of the sensors, metal systems have historically required sensors to be externally attached to the structure due to high temperatures during metal forming that will damage internal sensors [12]. This creates a major challenge in SHM aerospace applications as most aircraft components are metallic structures [6]. Some attempts have been made to utilize metal based additive manufacturing (AM) to embed FBG sensors. Selective laser melting (SLM) has been used to embed FBG sensors; however, residual stresses have caused sensor cracking and poor coupling to the metal matrix led to fiber slipping [25] [26]. Some investigations have obtained better AM embedment through preprocessing and coating of the fibers [27, 28, 29].

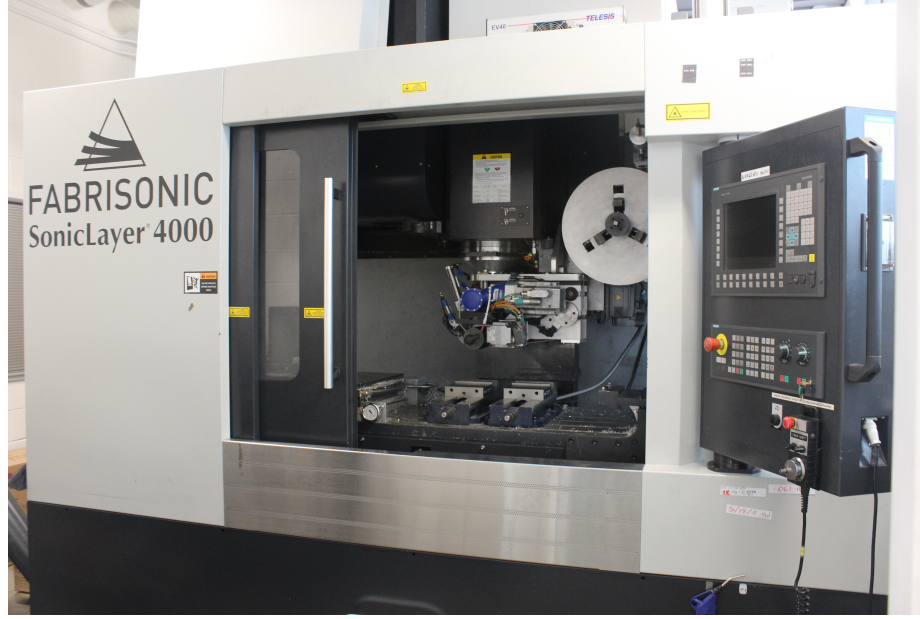


Figure 1.3: 9 kW Fabrisonic SonicLayer 4000 UAM system.

1.3 Ultrasonic Additive Manufacturing

Unlike most metal forming techniques, UAM is a low temperature process which allows for sensor embedment without preprocessing as it does not produce enough heat to damage most delicate sensors. In UAM, successive layers of thin foils are ultrasonically welded on top of each other to build up a metal part [30]. Combined with an incorporated CNC machine, subtractive operations allow for internal features and net shape final parts. UAM builds are accomplished by creating solid-state bonds between successive layers of metal and a metallic baseplate due to direct metal-to-metal contact under large normal forces. This contact is caused by applying ultrasonic vibrations (~ 20 kHz) provided by two transducers to a thin foil while subjecting it to high mechanical loading. The combination of ultrasonic scrubbing and normal force

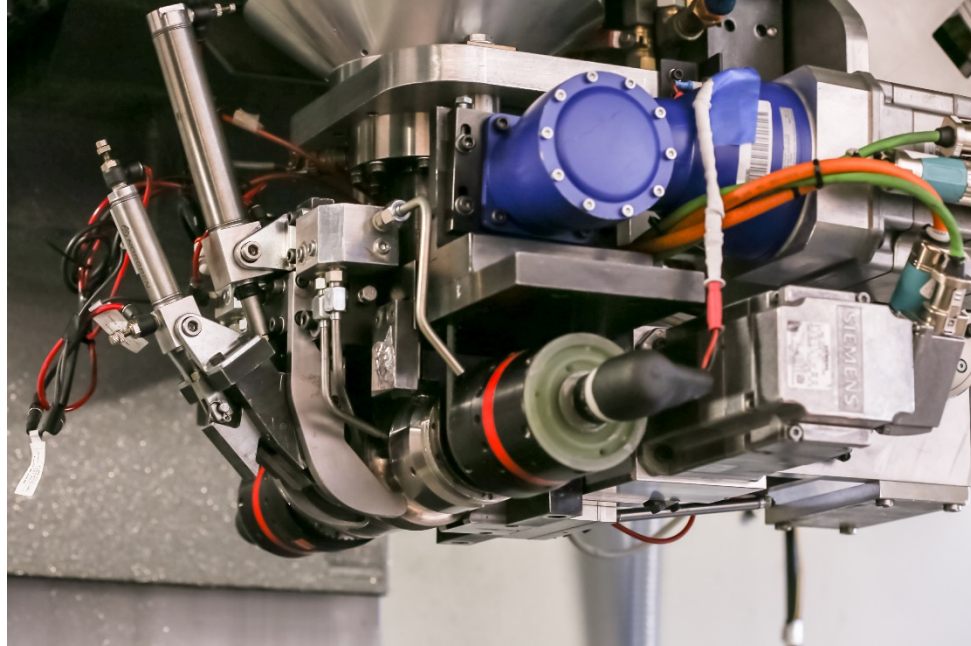


Figure 1.4: Welding assembly of a 9 kW Fabrisonic SonicLayer 4000 UAM system [33].

cause a number of effects that result in the faying surfaces to bond. The oxide layer and any contaminants are broken up and surface asperities between the substrate and foil surfaces plastically deform due to high shear rates, normal pressure, and localized temperature increases, which promotes diffusion from one interface to another [30] [31]. Ongoing research is underway to model the UAM process in order to predict the effects of changing process parameters and using new materials without time-consuming and complex tests [32].

The UAM system used in this thesis is the Fabrisonic SonicLayer 4000, pictured in Figure 1.3. The welding assembly can be seen in Figure 1.4. UAM can be used to join a variety of similar and dissimilar materials including aluminum alloys [31], steels [34], titanium [35], and carbon fiber composites [36]. The process of embedding fibers

into metal components has undergone significant research. Different types of fibers and sensors have successfully been embedded using UAM for structural reinforcement [35]. Temperature sensitive fibers of nickle titanium shape memory alloy embedded into aluminum structures have been demonstrated to alter the thermal expansion of the entire component [37]. Through machining operations performed on the foil before welding, electronic circuitry has been embedded using UAM [38]. Different processes of using UAM to embed fiber optic cables have also been investigated [39, 40]. Commercial FBG sensors embedded into metal through UAM have been shown to accurately track internal strain demonstrating the high potential of future SHM application [33, 41, 42, 43]. Plastic flow around UAM embedded fibers has been previously demonstrated, which leads to strong friction based coupling between the fibers and metal matrix [44].

The main process parameters in UAM are vibration amplitude, downward normal force, weld speed, and temperature [31]. In general, increasing the energy imparted by the UAM machine will improve weld quality. This means increasing normal force, increasing vibration amplitude, increasing temperature, and decreasing weld speed will improve weld quality. However, operating at extreme parameters can result in the foil welding to the horn instead of the baseplate. Consequently, some balance is required to avoid this risk and achieve an ideal weld quality. Future horns could be made of new materials or have special coatings to discourage this process [35]. While early UAM machines had a maximum weld power of 1 kW, newer machines, including the one used in this thesis, have a maximum weld power of 9 kW, allowing significantly stronger welds.

1.3.1 Dissimilar Material Joining in UAM

One capability of UAM is the ability to join dissimilar materials. A number of different material combinations for UAM have been researched. Softer materials are generally easier to weld, which resulted in most initial UAM research being performed with AL 3003 and Cu 1100 [45, 46, 47]. With the introduction of the 9 kW UAM systems, welding with harder materials became possible. Aluminum 6061 became the standard in UAM builds as new material combinations and machine parameters are researched further. In particular, there has been success welding with 4130 stainless steel [34].

An interesting challenge when welding with dissimilar materials, is that in cases of very hard materials, the foil will most likely bond to the horn at parameters high enough to cause welding. However, it is possible to weld harder materials onto softer ones using novel techniques. For instance, a titanium foil can be welded onto aluminum because the titanium preferentially welds to the aluminum instead of onto the harder steel horn. Therefore, for multiple layer builds, aluminum 1100 and commercially pure titanium bilayers have been successfully welded with UAM [35]. In this process, two layers are welded at a time, with the horn pressing down onto the titanium, which is above the aluminum layer. This arrangement can be seen in Figure 1.5.

This process is especially relevant to the aerospace industry where titanium is a common component due to its high strength and low weight [48]. An important titanium alloy in aerospace is Ti-6Al-4V (containing 6% aluminum and 4% vanadium), where significant research is pursuing Ti-6Al-4V powder bed fusion techniques for complex aerospace components [49]. Therefore, an investigation was conducted into

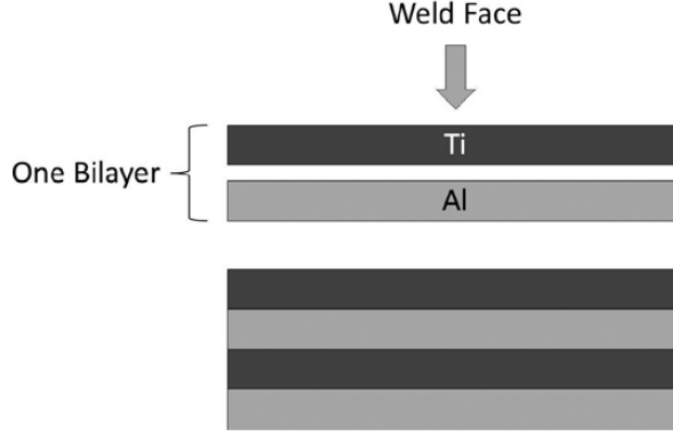


Figure 1.5: The bilayer configuration used for Al/Ti welding processes [35].

possible parameters for welding onto a Ti-6Al-4V component, provided by Moog, Inc. Previous studies had been performed on commercially pure titanium, which is much softer than Ti-6Al-4V [50]. Furthermore, previous studies increased the ambient temperature to 200°C, which would not be possible if fiber optic cables were to be embedded. This pilot study was able to successfully weld aluminum 1100 and titanium ATI 425 bilayers onto a block of Ti-6Al-4V made through powder bed fusion at room temperature as seen in Figure 1.6. The UAM process parameters used to achieve this successful weld are a weld force of 5 000 N, weld speed of 21.2 mm/s and a vibration amplitude of 24 μm

1.4 Method of Embedding Sensors through UAM

Test specimens were built using UAM on a Fabrisonic SonicLayer 4000. This study used aluminum 6061 due to the well documented machine parameters for creating high quality bonds that exist for this alloy [51]. The baseplate was of the T6 condition

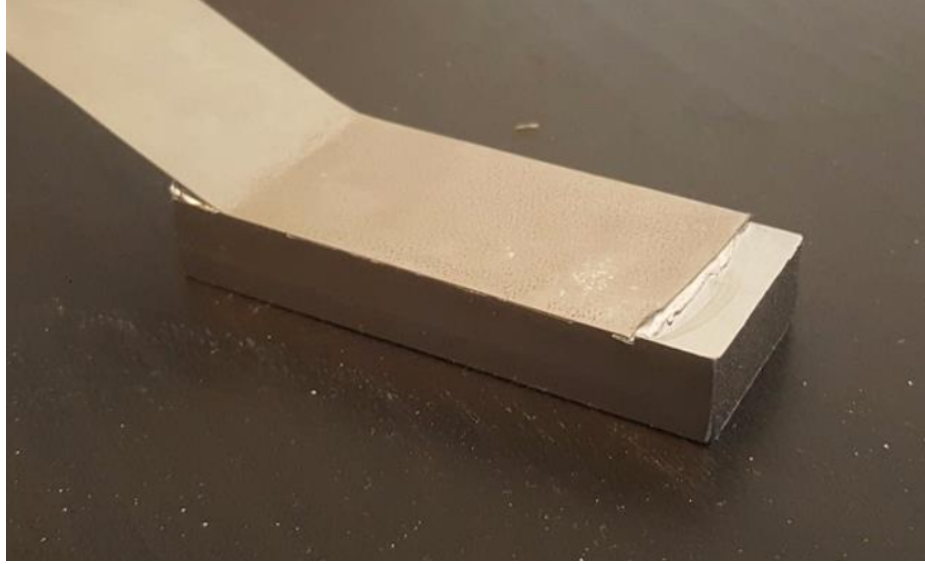


Figure 1.6: Successful UAM weld of a Al/Ti bilayer onto a block of Ti-6Al-5V made through powder bed fusion.

and the 0.154 mm thick foil layers were of the H18 condition. In this investigation, UAM parameters used for sample fabrication are 5 000 N downward force, weld speed of 84.6 mm/s, and a vibration amplitude of 32 μm .

The general coupon fabrication process is outlined below and shown in Figure 1.7. First, one layer of tape was welded onto the baseplate using UAM. Next, a 0.254 mm by 0.254 mm channel was cut using a ball end mill at the location the fiber will later be embedded. Channels of different sizes can be machined for different sensors. The channels help to avoid cross-sectional loading and sensor deformation during welding [41]. The sensors were then placed into the channels with the remaining fiber exiting the sample and additional layers were welded on top to fully encapsulate the FBG sensors at the center of the coupon geometry. After the sensor encapsulation, CNC

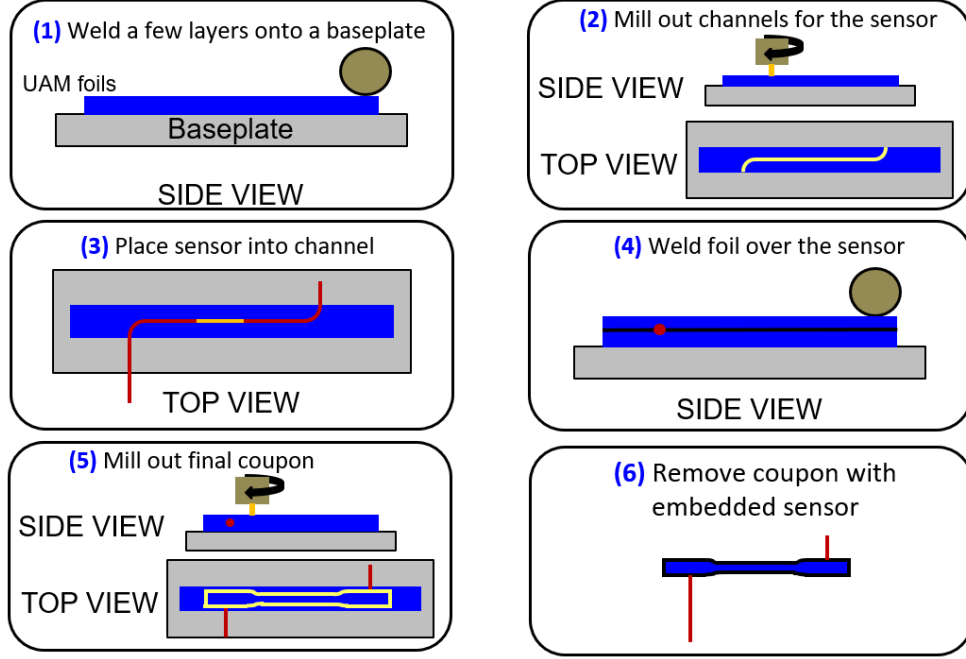


Figure 1.7: The basic procedure for embedding sensors into metal through UAM.

milling operations were used to build the final sample geometry with the FBG sensor embedded halfway through the sample.

The specific geometries created are outlined in the sections below and vary for the different tests. The embedded FBG sensors were examined using a polarization controller for changes in their birefringence and polarization response, as it had been documented that the existence of birefringence induced noise is indicative of a small channel and possibly of poor bond quality [41]. Birefringence is when the refractive index is dependent on the polarization light. Deformed optical fibers can exhibit birefringence that is manifested as high levels of noise in the FBG signal. An example of a backlit cross section of a UAM embedded FBG demonstrating core survival can be seen in Figure 1.8.

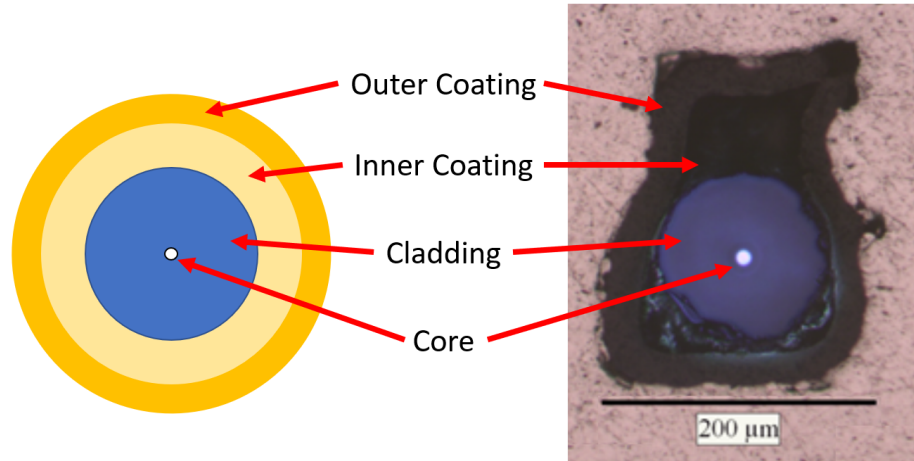


Figure 1.8: Cross section of a drawing of an optical fiber compared to a backlit cross section of a UAM embedded optical fiber [33].

1.4.1 Laser Pointer Demonstrator

In order to create a demonstration of the unique ability of UAM to embed fiber optics (and other delicate sensors), a laser pointer demonstrator was constructed. Using the process outlined above, a 3 ft fiber optic cable with one side ending in a collimator lens was installed into aluminum [52]. A fiber optic visual fault detector was directly attached to the other side of the cable. The fault detector sends light down the fiber and the lens collimates the light back into a directed laser point.

After additively building up a 3 inch by 1 inch aluminum block, channels were cut to house a collimating lens and the fiber optic cable. The fiber was made to bend 90 degrees and exit the aluminum block. The lens was then installed, Figure 1.9 and additional layers were welded to encapsulate the lens and fiber, Figure 1.10. Final machining operations were then performed to remove the component from the

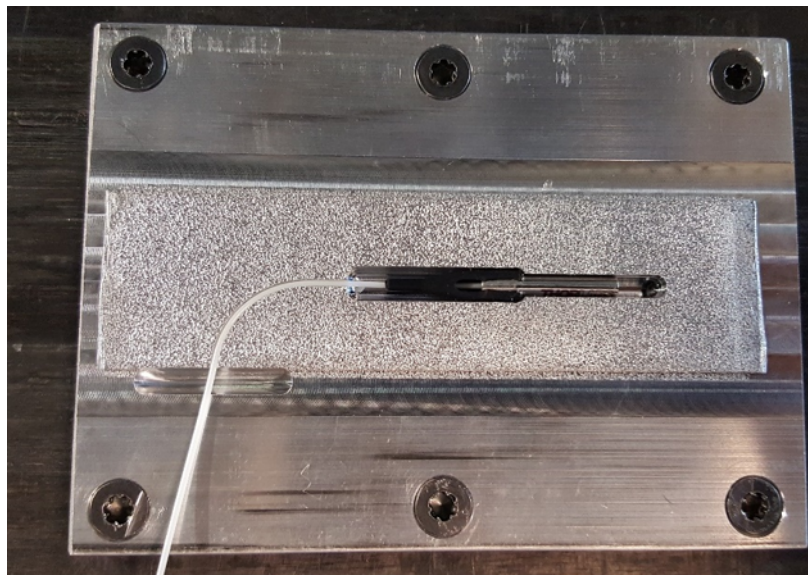


Figure 1.9: The lens and fiber have been installed into the channels of the UAM structure. Note the rough surface texture around the embedded sensor which is imparted by the UAM process after welding each layer. This texture can be easily machined away.

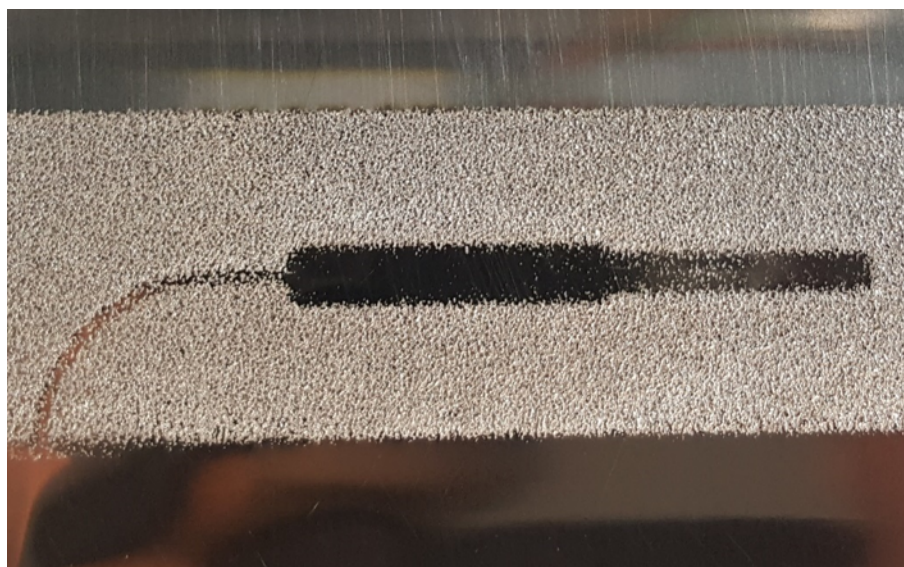


Figure 1.10: The welds over the lens and fiber show no tearing in foil and complete encapsulation. A smooth texture occurs above channels since no welding is occurring at those locations.

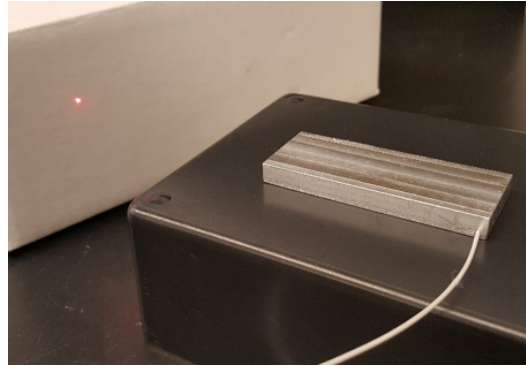
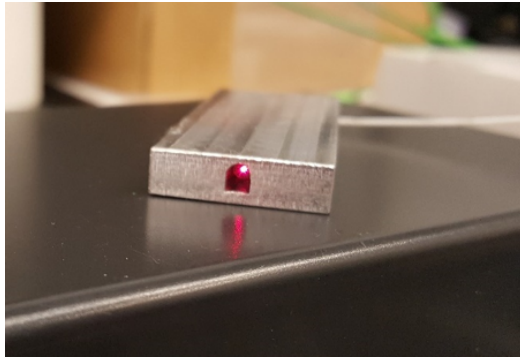
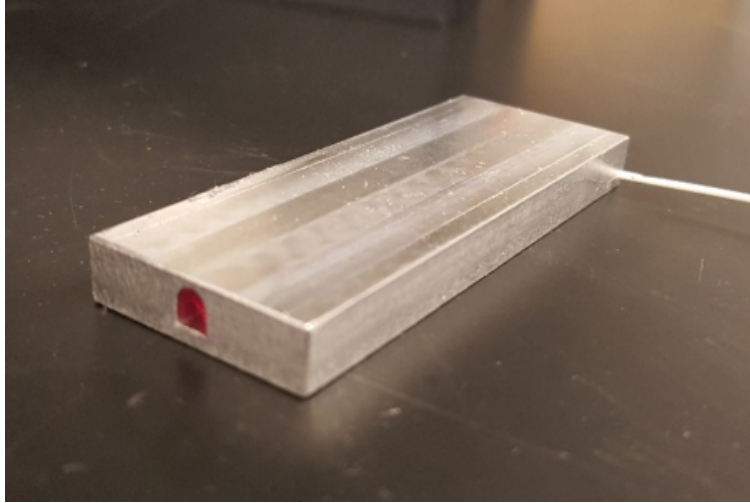


Figure 1.11: Different angles demonstrating the completed and fully functional laser pointer demonstrator.

baseplate. As demonstrated in Figure 1.11, the device successfully functions, demonstrating that the process defined above can be used to embed fully functioning fiber optic components.

1.5 Experimental Test Equipment

A number of different research instruments and software were used throughout this investigation and are discussed in detail below.

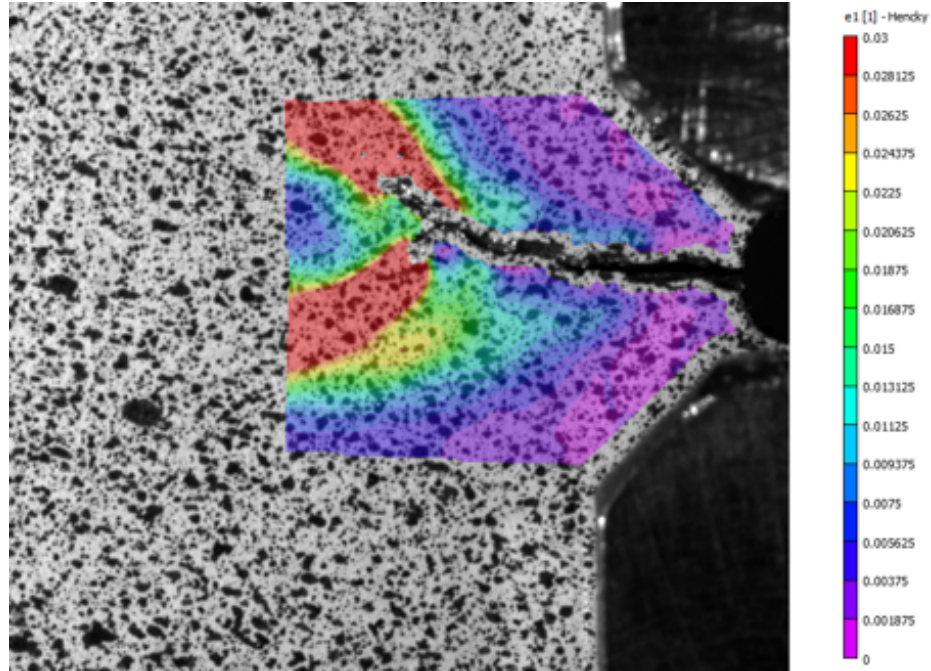


Figure 1.12: A strain field during the cyclic loading of a CT specimen generated through DIC.

Digital Image Correlation (DIC) is an image processing technique where a speckling pattern is placed on a sample and images are taken throughout testing. DIC analysis tracks the movement of individual speckles and determines the strain field of each image. DIC was performed using a 5 megapixel camera with a 100 mm lens controlled by Vic-Snap 9 Image Acquisition software from Correlated Solutions. An example DIC strain field can be seen in Figure 1.12 which shows a strain field overlaid on close up image of a compact tension specimen just before failure.

An MTS Criterion Model 43 load frame was used for all tensile testing performed in this investigation. The loading profile was created using the MTS TW Elite software and a National Instruments 9215 data acquisition module gathered the data.

For experiments performed above room temperature, a Thermo Scientific Thermolyne furnace was used. The temperature was verified using a K-type thermocouple and strain was verified using HPI Inc. HFK-12-125-6-ZCW high temperature strain gauge that was fixed with epoxy to the coupon. Data was recorded using a National Instruments 9215 data acquisition module.

FBG strain sensors, the wavelength interrogator, and analysis software were provided by Moog, Inc. The interrogator is an Insensys (Moog, Inc.) model OEM 1030 and was originally designed for wind turbine strain monitoring. The interrogator is able to read peaks from multiple gratings in up to three separate fibers. There are a number of nuances that are important to understand when operating the interrogator. First, the interrogator functions by initially detecting wavelength peaks in each channel, and then tracking the change of each of those peaks. When a sensor undergoes non-uniform loading, the grating can produce multiple peaks causing the interrogator to hop between different peaks. It is therefore important to install the FBG sensor so that it experiences uniform loading during operation whenever possible. Furthermore, the interrogator is limited to sensing wavelengths between 1545 nm and 1555 nm. Finally, the interrogator runs off of the connected computer's internal clock, which means additional processing is required for time independent data. When time synchronization with other data inputs was necessary, a custom built analog to digital converter would convert the serial wavelength output of the interrogator to a voltage, which could then be input into the data acquisition system. The converter is built using a Teensy 2.0 USB development board with custom firmware. The converter can be operated in full tensile mode or in tension and compression depending on the application. Note the nominal voltage of the converter is set to the value when the

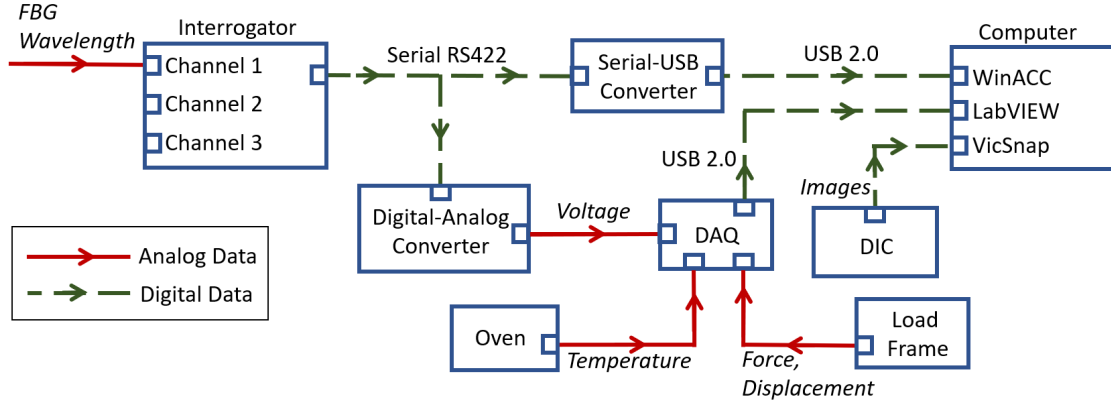


Figure 1.13: Connection diagram of the various equipment, software and signals used in this thesis. Analog signals are shown with a solid red line and digital signals are shown with a green dotted line. Not all experiments performed used every piece of the equipment shown.

converter is first turned on, which is not necessarily the nominal wavelength of the fiber.

Figure 1.13 illustrates the connection diagram associated with this investigation. Analog data of the FBG peak reflected wavelength is received by the interrogator, which then outputs the result as serial RS422 digital data, which can be received directly by a computer with the WinACC software after a serial-USB converter. The serial data is also directed to the digital-analog converter circuit, where it is converted to an analog voltage and sent to the NI DAQ. The DAQ also receives analog inputs of temperature, from oven thermocouples (during elevated temperature testing), and force and displacement, from the load frame (during tensile testing). The DAQ synchronizes the signals and outputs a digital signal through USB to the computer for processing by LabVIEW. Finally, the DIC system sends images to the computer

for processing by the Vic-Snap software. Any post processing of data was performed using MATLAB.

1.6 Problem Statement

For new industries to take full advantage of the benefits of SHM, advancements in sensing technologies are necessary. In particular, SHM of metal structures currently requires exterior attached sensors, which is not viable for many applications such as aerospace. Therefore, research into encapsulation of sensors into metal is crucial to expand SHM applications. FBG sensors are common in SHM; however, their delicate nature makes encapsulation difficult. Traditional metal forming techniques require melting of the metal, which would consequently damage virtually all sensors. UAM presents the unique opportunity to form full, complex metal parts without the elevated temperatures that could damage sensors. Previous work has demonstrated the ability of FBG sensors to accurately detect strain after encapsulation into metal using UAM. The work presented in this thesis demonstrates the first exploration into the potential of UAM embedded FBG sensors for SHM applications.

1.6.1 Thesis Outline

In this thesis, the use of UAM embedded FBG sensors in SHM applications is investigated. First, the effects of fiber embedment on the mechanical characteristics (tensile strength and fatigue durability) of metal coupons is investigated in Chapter 2. In Chapter 3, the results of the damage detection potential of UAM embedded FBG sensors is presented. FBG sensors were embedded into compact tension (CT) specimens to determine their effectiveness in detecting crack growth and initiation. Chapter 4 examines embedded FBG sensors that were thermally tested to investigate

the range of operational temperatures. Conclusions and future work is discussed in Chapter 5.

Chapter 2: Mechanical Properties of Metal with Embedded FBG Sensor

For FBG sensors to be used in health monitoring applications, it is necessary to understand the impact of the fiber inclusion on the mechanical characteristics of the metal. Therefore, two experiments were performed to examine this relationship. The first study examines how coupons with and without a longitudinally embedded fiber behave under tensile loading. The second study examines the fatigue properties of coupons with embedded fibers.

2.1 Tensile Properties

In this study, the tensile properties of UAM build samples with and without embedded fibers were examined. Four types of Al 6061 samples that underwent tensile loading until failure were compared to examine the effect of fiber inclusion on mechanical properties.

2.1.1 Experimental Methods

This experiment followed the standards outlined in ASTM E8 [53]. Rectangular cross section sub-sized samples were constructed using UAM in accordance with the standards. The geometry can be see in Figure A.1. A control sample was made using

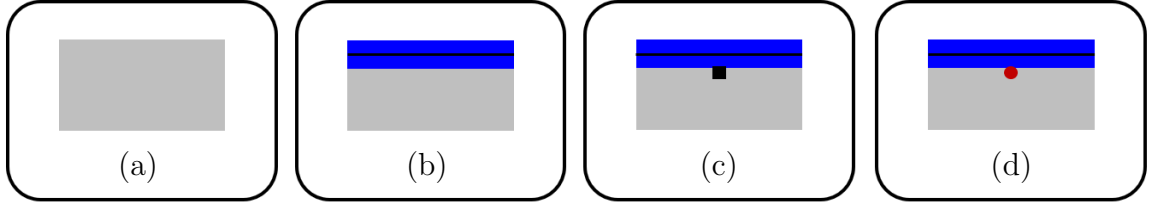


Figure 2.1: Cross sections of the four coupon geometries that underwent tensile testing: (a) bulk Al 6061-T6, (b) UAM control, (c) empty channel, (d) embedded fiber. Al 6061 is shown in grey, UAM layers are shown in blue, the channel is shown in black, and optical fiber is shown in red.

only bulk Al 6061-T6. For the other three samples types, an Al 6061-T6 baseplate was used with two layers of UAM H18 foils welded on top. These UAM samples were divided into three configurations: (1) solid, (2) with an empty channel, and (3) with an embedded fiber. The cross sections of the four coupons tested is illustrated in Figure 2.1.

Samples were installed into an MTS Criterion Model 43 load frame and the displacement and force were recorded using a National Instruments 9215 data acquisition module.

2.1.2 Results and Discussion

The individual sample results can be seen in Figure 2.2 and major mechanical features are summarized in Figure 2.1. These results show insignificant differences between the four sample types. While the bulk aluminum samples do appear slightly stronger than the other samples, each test remains within the expected strength range of 6061 aluminum [54].

Table 2.1: Summary of tensile test results.

Coupon Type	Sample #	UTS [MPa]	Elongation [%]
Bulk	1	314.4	0.2244
	2	311.9	0.2498
	3	306.1	0.2084
	Mean	310.8	0.2275
	STD	4.25	0.0209
UAM	1	299.8	0.2003
	2	299.2	0.1945
	3	297.2	0.1798
	4	301.3	0.1779
	Mean	299.38	0.1881
	STD	1.70	0.0110
Channel	1	296.3	0.2012
	2	296.1	0.1960
	3	299.4	0.1898
	4	297.3	0.1861
	Mean	297.28	0.1933
	STD	1.51	0.00668
Fiber	1	303.1	0.2372
	2	301.6	0.1899
	3	296.2	0.1750
	Mean	300.3	0.2007
	STD	3.63	0.0325

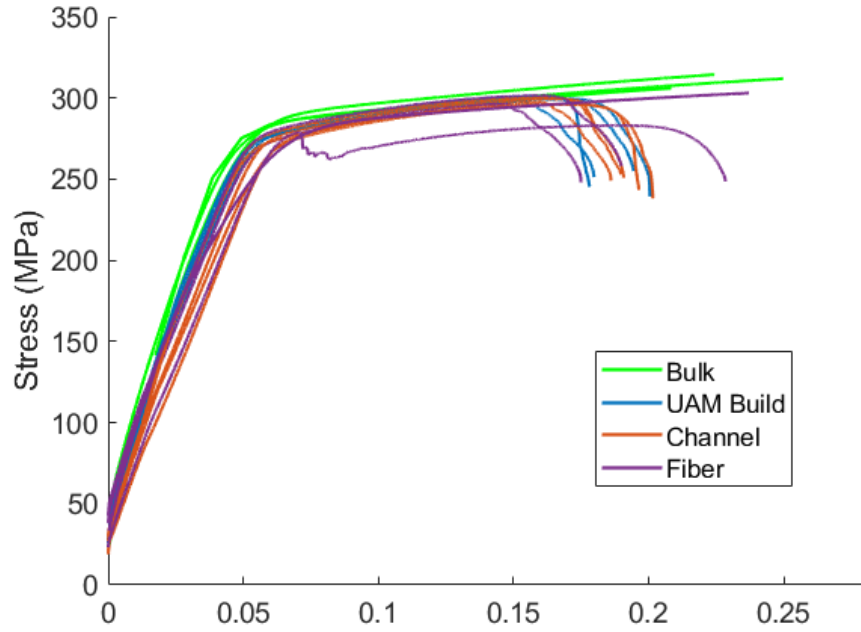


Figure 2.2: Tensile testing results from all samples.

Results from a finite element analysis are presented in Figure 2.3 which modeled the effect of a fiber on the tensile properties. Negligible difference was found in the FEA analysis.

These results suggest that the inclusion of a fiber through UAM has little effect on the tensile properties of aluminum 6061-T6. There are a number of additional factors to consider. First, the foil used was in the as-rolled H18 condition which is weaker than the T6 condition. Using a higher volume fraction of H18 would likely have a larger effect on the strength of the specimen. However, it is possible to weld with heat treated T6 foil, which could ameliorate this issue. Additional test could include samples with varying volume fractions of UAM aluminum T6 layers to fully quantify the impact of UAM on the tensile properties. As demonstrated in the test

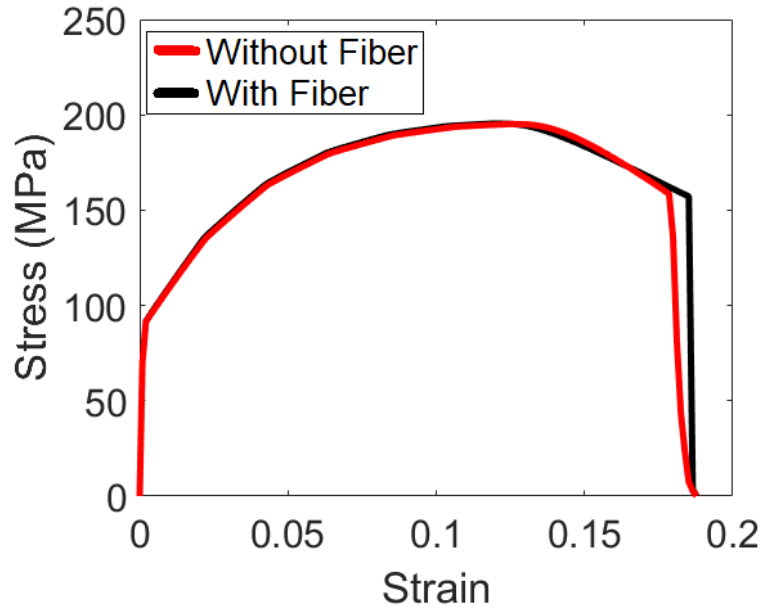


Figure 2.3: Finite element analysis of tensile testing with and without an embedded fiber.

result and FEA analysis, the small cross-sectional area of the fiber leads to very little effect on the overall strength of the sample. Further research could also focus on the relationship between fiber orientation and tensile strength.

2.2 Fatigue Properties

In this investigation, the fatigue properties of samples with embedded fibers were examined. The goal was to determine the relationship between maximum cycle strain and number of cycles before failure to create S-N curves.

2.2.1 Experimental Methods

This experiment followed the procedure outlined in ASTM Standard E466-15 [55]. Both the ASTM E739-10 standard and the ASTM manual on Statistical Planning and Analysis for Fatigue Experiments were also used in the design of this experiment [56, 57]. Three types of samples were constructed: (1) bulk Al 6061-T6, (2) with an embedded fiber, and (3) with embedded fiber that had undergone the T6 heat treatment. The fibers were installed longitudinally down the gauge region of the samples. As with the tensile testing, the samples with a fiber had two layers of H18 foil above the channels. All burrs were carefully removed and the edges were sanded to reduce the effects of surface defects on the fatigue life.

In order to achieve higher repeatability, each sample type was tested at four different stress levels multiple times. Complete separation was used as the failure criteria. Samples were cyclically loaded at a rate of 50 Hz with pure tensile loading, thus a stress ratio of $R = 0$.

2.2.2 Results and Discussion

Figure 2.4 shows the results from fatigue testing with each data point the average of multiple trials. The key feature to note is that due to the high variability inherent in fatigue testing, there was no major outlier between the specimen types. The grey dotted line depicts the lower boundary of Al 6061 where the literature predicts 97.7% of trials will be to the right. All of the trials were to the right of this boundary, and thus fall within normal expectations of bulk aluminum 6061. The trend lines of both UAM samples appear to be slightly lower than the bulk literature and tested trend lines; however, this difference is too small to attribute to a weaker structure.

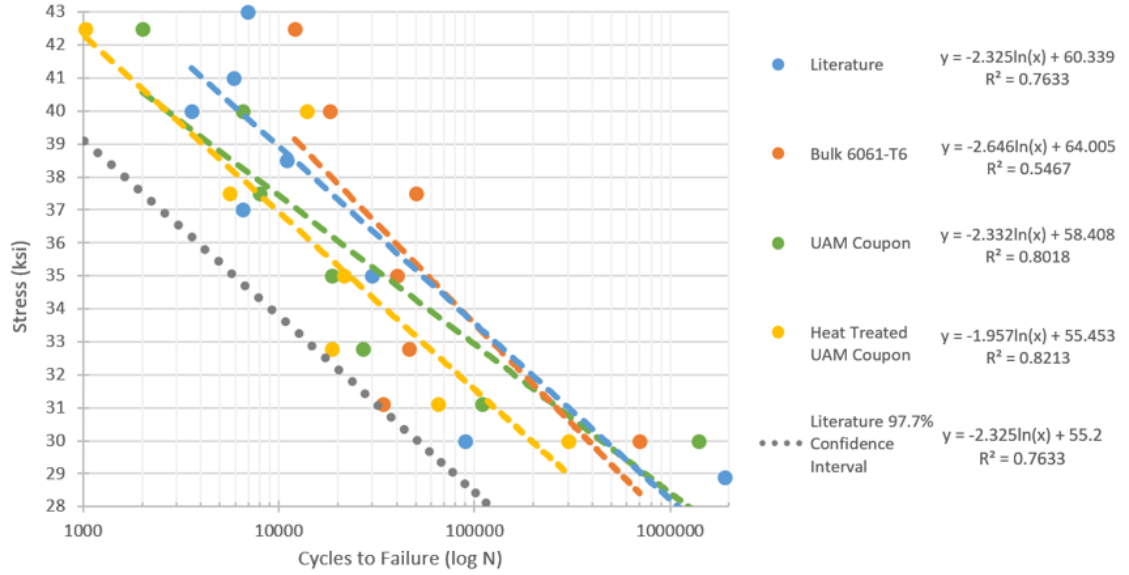


Figure 2.4: Results from fatigue testing. Literature values from MMPDS [54]. All UAM samples contain an embedded fiber.

In order to quantify any differences between bulk aluminum and aluminum with an embedded fiber, more testing at new stress values with higher repeatability is required. The major limitation with fatigue testing is the difficulty in conducting tests due to the significant number of cycles required at lower stress tests. It was for this reason that many of the trials were performed at higher stress levels. For future tests, it would be valuable to use the load frame under strain control and produce ε -N curves, which tend to be more consistent at lower cycle regions. It would also be valuable to determine the endurance limit of UAM samples with embedded fiber optic cables. Further research could also focus on the relationship between fiber orientation and fatigue properties.

Chapter 3: Crack Propagation Detection and Prognostic Analysis

3.1 Crack Propagation Tracking and Early Crack Detection

3.1.1 Experimental Methods

Tests were conducted to investigate the ability of UAM embedded FBG sensors to detect cracks in samples. The geometry of the coupons and testing procedures were based on ASTM Standard E647: Standard Test Method for Measurement of Fatigue Crack Growth Rates [58]. This test involves the cyclic tensile testing of notched compact tension (CT) specimens to induce crack growth. A clevis-pin system was designed to be held in the load frame and attached to the CT specimen. A drawing of the of the CT specimen used in this testing is shown in Figure A.2. Due to machining limitations, the tip of the notch was not machined to the radius listed in the ASTM Standard. However, this was deemed irrelevant to the following experiments as the material properties were not being characterized, which require more consistent crack development.

Although the purpose of ASTM E647 is for material characterization, we were interested in the strain signal throughout the lifetime of the coupon. For comparison to the strain measurements made by embedded FBG sensors, strain was also measured

through DIC. After a set amount of cycles, the load frame triggers the DIC to capture an image by having a minimum tensile load slightly smaller than the other cycles. The DIC calculated vertical strain field in the region of the embedded FBG was averaged and used as a comparison to the FBG signal. Crack growth was measured optically using images taken by the DIC system. The length of each pixel corresponded to 0.0054 mm. The experimental setup can be seen in Figure 3.1. There were two main investigations into crack propagation with CT specimens outlined below: (1) crack initiation and strain tracking, and (2) prognostic analysis.

This experiment closely followed the procedure of ASTM E647. The CT specimens with embedded FBG sensors were installed into the load frame and loaded cyclically until the crack reached 1 mm. This pre-cracking phase alternated between tensile loads of 200 N and 2700 N with a sine wave and a period of 0.25 Hz. After the crack was measured to be greater than 1 mm, the main testing phase began, where the crack was grown until sample failure with the maximum load reduced to 1800 N. The DIC system was used to take an image at the peak load every 8 cycles during the pre-cracking phase and every 20 cycles during the remainder of the test. The FBG sensor collected data throughout the entire testing procedure. Data from the pre-cracking phase was used to determine the minimum crack size detected by the FBG sensor. The mean was found for each set of peaks between DIC imaging. A distribution, which is assumed to be normal, of the mean peak values for each set was found for the region before crack initiation occurred. Normal operation (without defects) was arbitrarily defined as set peaks within three standard deviations from the distribution mean. Therefore, we can define the first set whose mean exceeds these bounds to be the earliest that the FBG can detect the crack initiation. Industrial

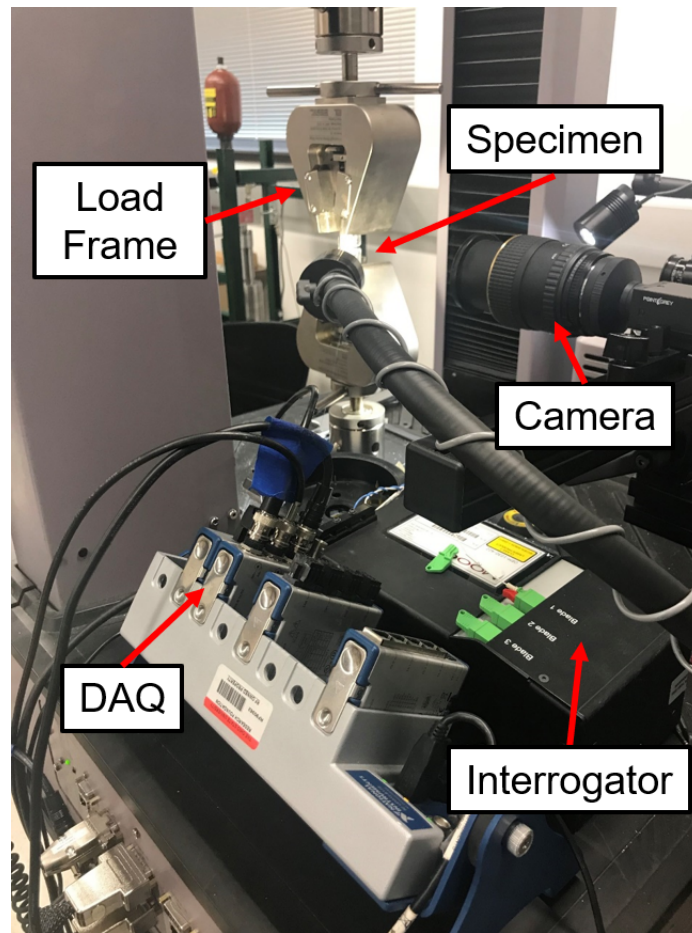


Figure 3.1: Experimental setup showing a CT coupon installed in the load frame.

applications would have significantly larger data sets and could use more advanced AI techniques for determining the presence of defects, which was beyond the scope of this exploratory study. Data from the main testing phase was used to determine the ability of FBG sensors to track strain throughout the growth of the crack.

3.1.2 Results and Discussion

The raw strain found by a UAM embedded FBG sensor for the entire life of the CT specimen can be seen in Figure 3.3. As the crack grows there is a clear large increase in strain, signifying strain transfer during the growth of the crack. The large jumps in data occurred just before failure and are mostly likely the result of wavelength hopping that may have occurred as the crack approached the fiber [59].

The early detection of cracks is an important aspect of SHM sensors as the ideal sensor can detect and track defects long before catastrophic failure occurs. Data from the pre-cracking phase was examined to determine how small of a crack the UAM embedded FBG can detect. The pre-cracking phase in its entirety is shown in Figure 3.4, which ends at the red arrow in Figure 3.3. The red square highlights a detailed view shown in Figure 3.5, where the lower cycles used to trigger the DIC image capturing is clear. MATLAB peak detection was used to identify the maximum values of each cycle as illustrated in Figure 3.6.

The peak identification function was performed over the entire pre-cracking data set (Figure 3.4) and only the peaks were plotted in Figure 3.7. Each time the minimum or maximum loads of the load frame were changed, there was a very small, but consistent decrease in the maximum and minimum points over the next few cycles. This effect was repeatable with different, FBG sensors, coupons and in compression

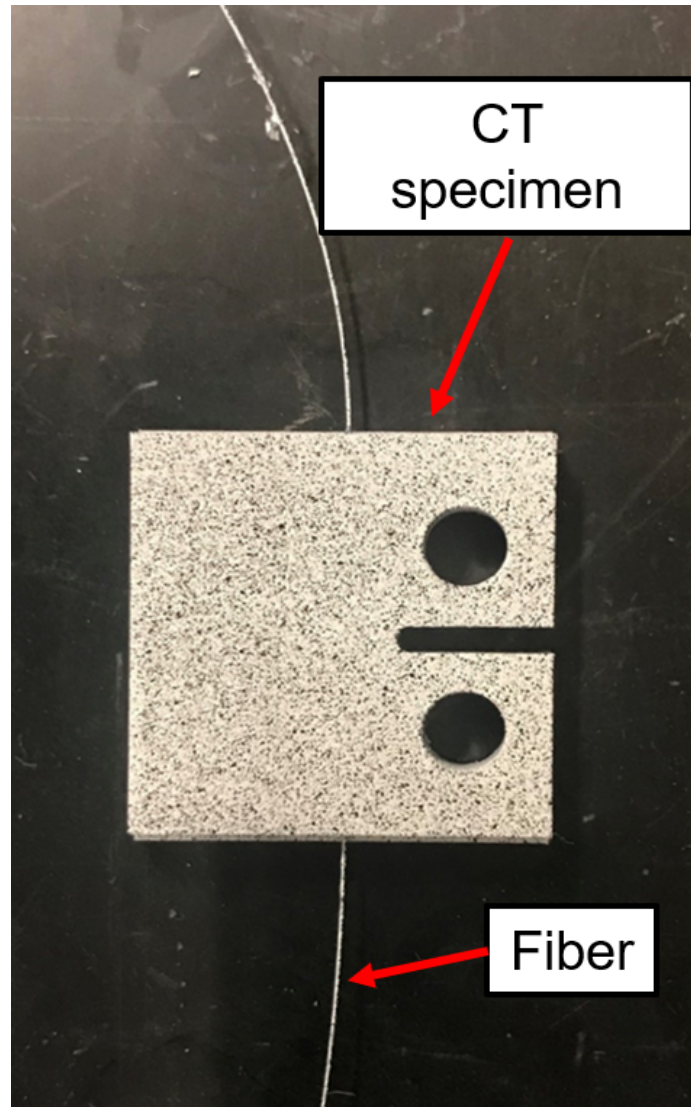


Figure 3.2: Compact tension (CT) specimen with one embedded FBG sensors built using UAM used in crack initiation and strain tracking testing. A fine speckle has been applied for DIC tracking.

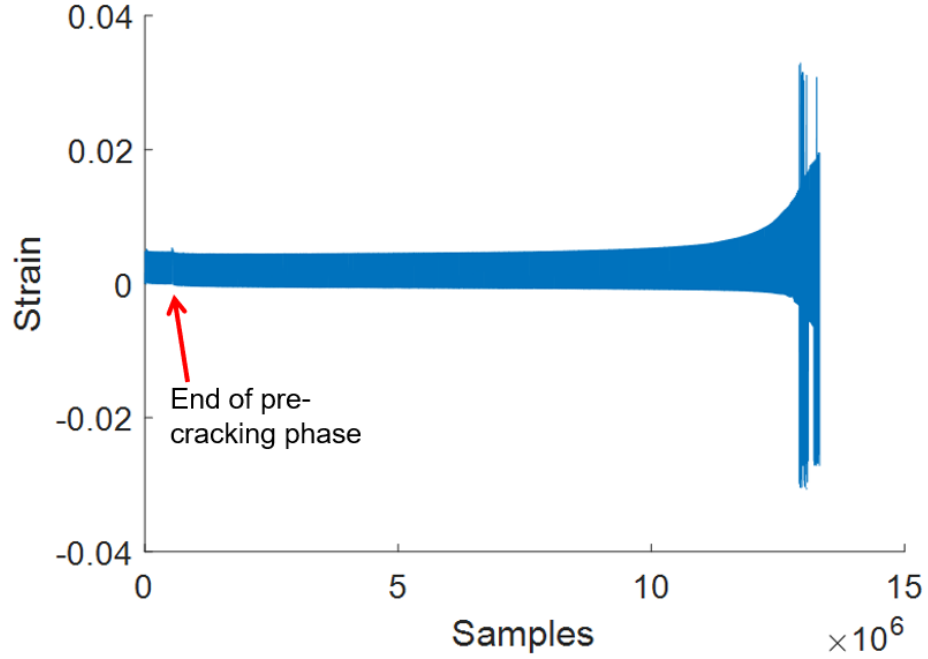


Figure 3.3: The raw FBG strain signal throughout the life of a CT specimen. The end of the pre-cracking phase is denoted by the red arrow. The vertical lines at toward the end of the sampling are likely artifacts of the FBG fiber slipping as the crack neared the embedded fiber.

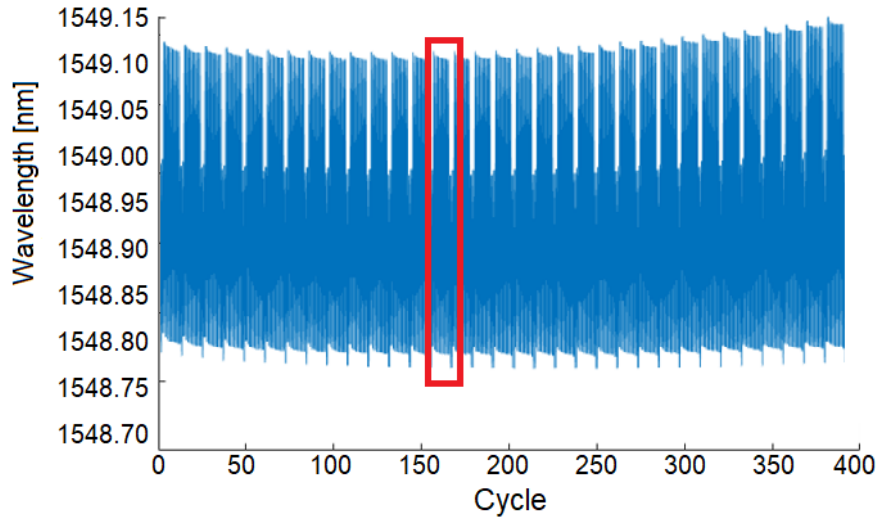


Figure 3.4: Peak reflected wavelength from FBG during the pre-cracking phase, extracted from Figure 3.3. The red box shows the range of Figure 3.5.

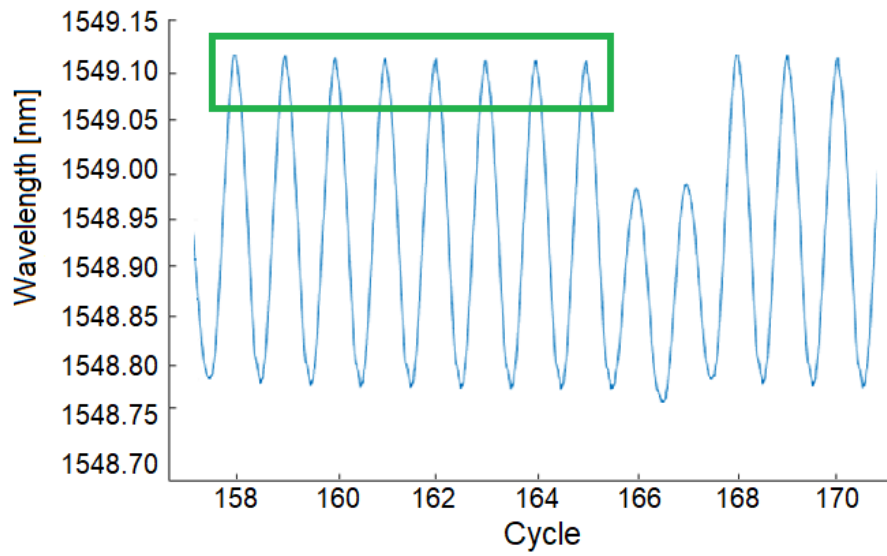


Figure 3.5: Detailed view of the red box in Figure 3.4, showing the strain over about ten cycles. Note the two lower cycles used to trigger the DIC.

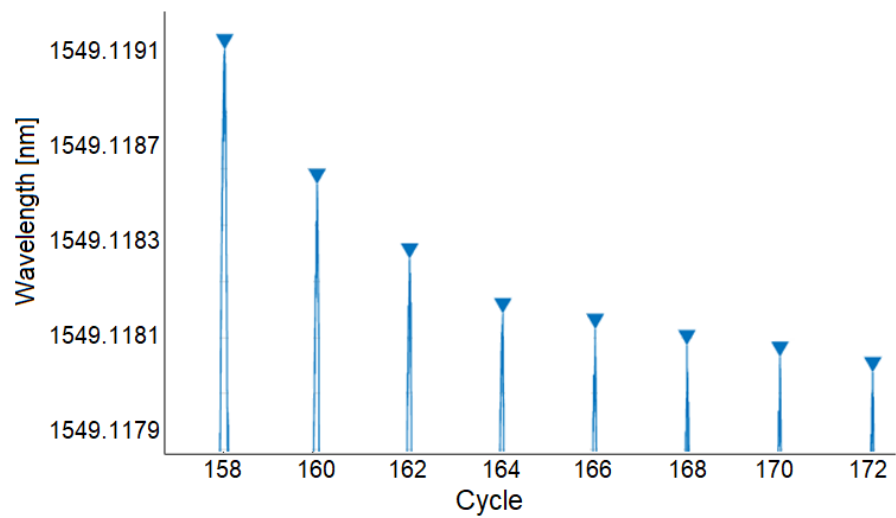


Figure 3.6: Detailed view of the green box in Figure 3.5, showing the maximum values of a set of 8 cycles. The peaks are marked with a triangle.

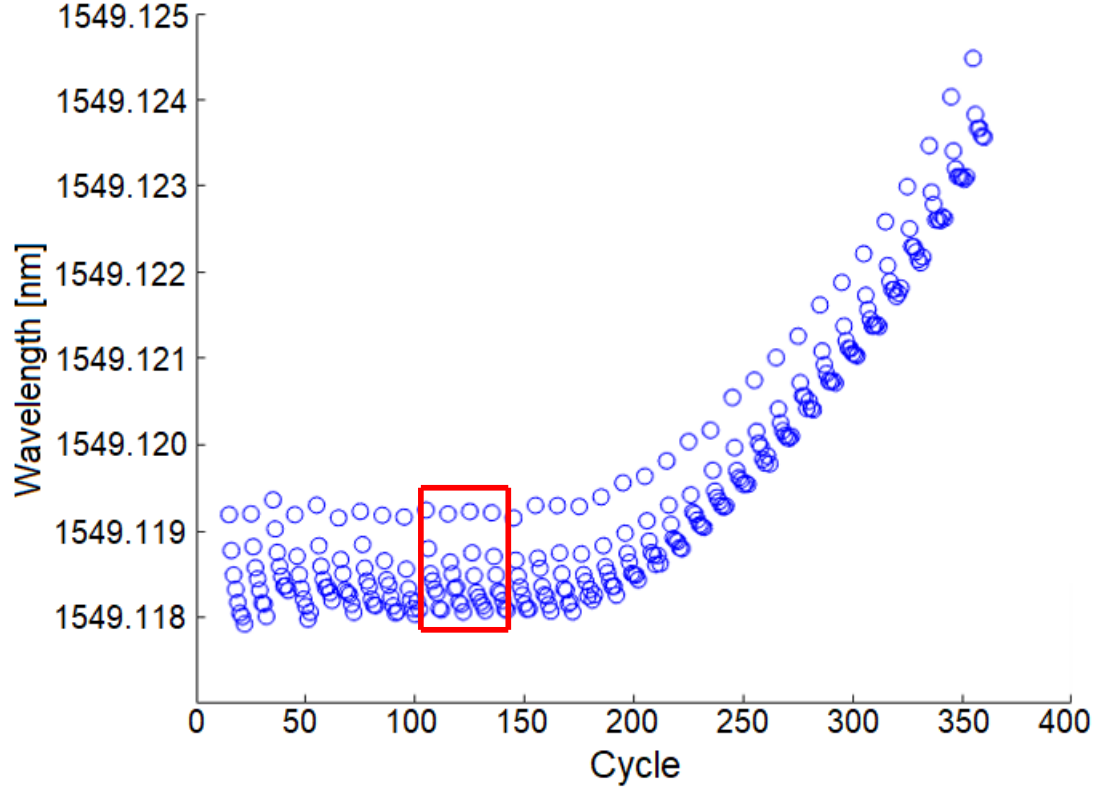


Figure 3.7: The peaks of the FBG strain signal during the pre-cracking phase. After every eight cycles, the DIC was triggered with a low peak (not shown). The red box shows the boundaries of Figure 3.8.

(albeit mirrored, with the peaks increasing). Examination of this phenomenon showed that this decrease in peak signal lasted consistently 20-30 cycles and that the load frame does not exhibit this signal. Additional investigation is underway to fully understand this effect, although it should be noted that this has little effect in practical applications as the actual strain difference is under $1 \mu\epsilon$. This strain relaxation could be the result of a viscoelastic effect from the acrylate coating or an artifact from the interrogator or triggering system.

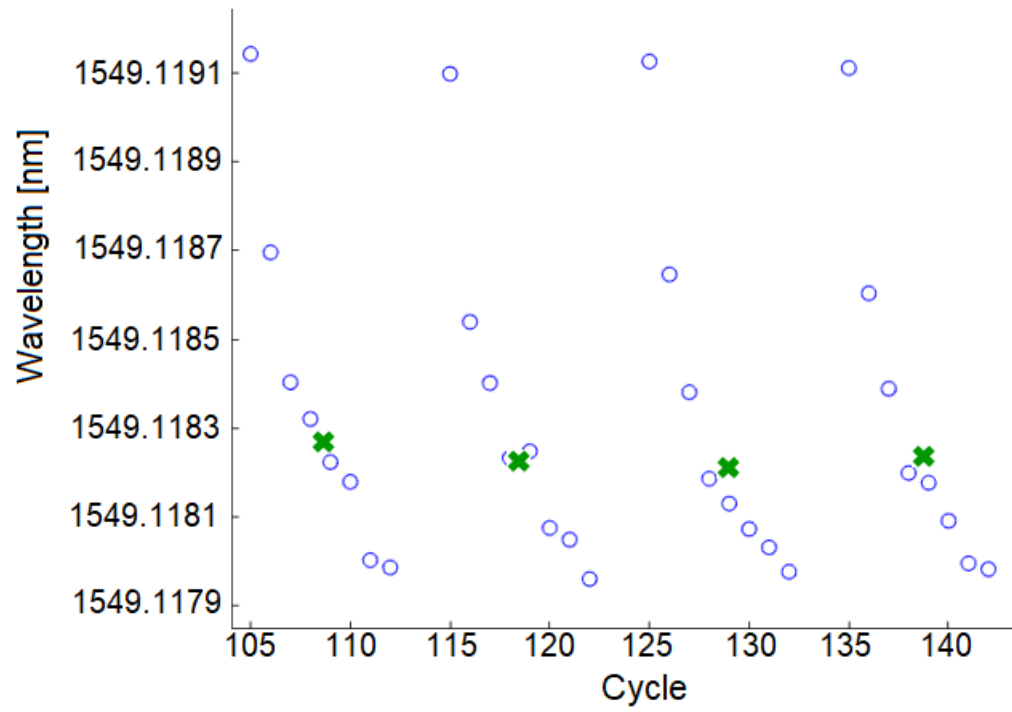


Figure 3.8: Detailed view extracted from red box in Figure 3.7 of peaks of the FBG strain signal during the pre-cracking phase are shown for four sets of eight cycles, The green x markers indicate the mean of each set.

Table 3.1: Length of crack in CT specimen at earliest detection using a UAM embedded FBG sensor 3 mm from notch. Ranges are due to crack entering a DIC speckle and consequently being unable to optically determine a precise endpoint.

Sample	Crack Size [mm]
1	0.335 ± 0.046
2	0.234 ± 0.054
3	0.291
Average	0.286 ± 0.033

The largest effect of this phenomenon, is that it increased the standard deviation of the normal peak distribution reducing the effectiveness of detecting crack initiation. In the following discussion, the group of peaks after a DIC triggering cycle will be referred to as a set. Instead of using individual peaks before crack initiation, the mean was calculated for each set of 8 cycles, as illustrated in Figure 3.8. Comparing the means of each set had a much smaller variation and allowed for a more precise measurement of crack detection. The mean of the sets before the crack caused any deviation in signal were used to define a normal distribution with a overall mean of 1549.1181 nm and a standard deviation of 0.0097 nm. We can define the first set that exceeds three standard deviations from this normal mean to be the earliest detection of a crack. The first set whose mean exceeds this range is during cycles 195 to 205 corresponding to a crack length of 0.332 ± 0.046 mm. This analysis was repeated for two additional samples and the results are presented Table 3.1.

This result illustrates the potential of embedded FBG sensors to detect early crack formation. Comparing this result to other non-destructive investigation (NDI) techniques used in the aerospace industry, shown in Table 3.2, highlights that the

Table 3.2: Comparison of early through crack length detection of UAM embedded FBG sensor to common aerospace NDI techniques [60].

Technique	Crack Size [mm]
UAM FBG	0.286 ± 0.033
Eddy Current	2.54
Penetrant	3.81
Magnetic Particle	6.35

UAM embedded FBG sensors perform at about an order of magnitude better than other methods.

It is noted that literature values are the minimum crack detected 90% of the time using the NDI techniques on large parts with unknown cracks. For FBG sensors to be viable alternative in industry applications, a strong understanding of where stress concentrations exist in the part and where cracks or defects will likely appear. This may require FEA analysis and fatigue testing of components to educate the placement of the FBG sensors. Furthermore, these tests were carried out by FBG sensors located 3 mm from the crack initiation spot. Further investigation of the effects of this distance could better inform FBG placement into parts. There may be a trade-off between a broader area that can be detected by the FBG and the size of crack when first detected.

The results from the main phase of testing provide strong evidence for ability of UAM embedded FBG sensors to accurately track strain as a crack propagates toward the sensor. Figure 3.9, Figure 3.10 and Figure 3.11 demonstrate very accurate strain tracking for most of the sample lifetime. At approximately 9500 cycles, the crack has grown to be over 3 mm long and consequently has passed the fiber. At this

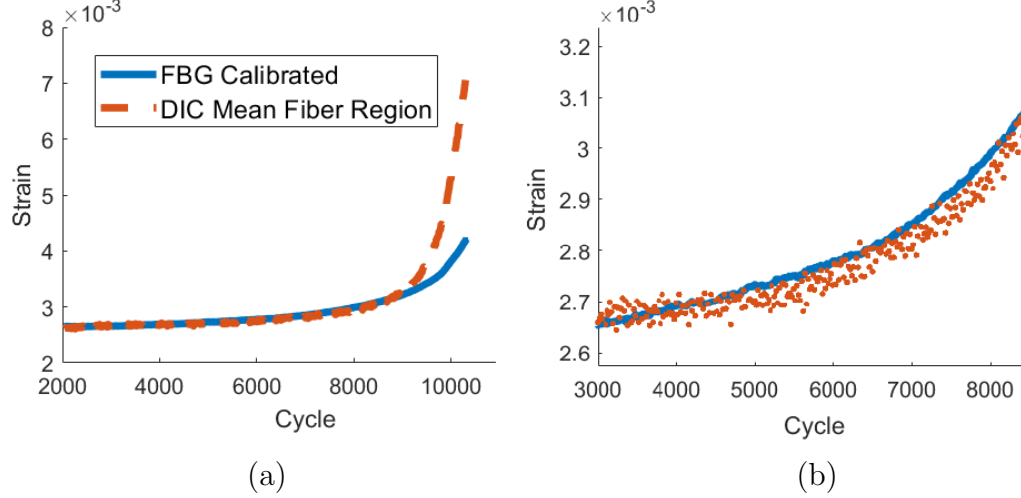


Figure 3.9: Vertical strain measurements from a FBG sensors embedded into a CT specimen through UAM and the average strain from DIC in the region of the FBG; (a) from the end of the pre-cracking phase (\sim cycle 2000) to sample failure (\sim cycle 10500); (b) detailed view of (a) approximately from cycle 3000 to 8500.

point the FBG strain begins to deviate from the DIC measured average strain. It is hypothesized that this occurs as the fiber begins to slip within the channel, reducing the value of the strain. Prior to this slipping, the FBG signal remains extremely accurate as illustrated in Figure 3.10. In the first 6000 cycles, a ten cycle moving average of the peak strain of the FBG stays within 1% of the DIC strain, and remains within 5% after 8000 cycles. UAM embedded FBG sensors are therefore a promising candidate for crack growth tracking in SHM applications.

3.2 Prognostic Analysis

3.2.1 Experimental Methods

In this experiment, a CT specimen was built with three embedded FBG sensors spaced 3 mm, 6 mm and 9 mm from the notch as pictured in Figure 3.12. Next, cyclic tensile testing was done with a sine wave and a period of 0.25 Hz. The load profiles

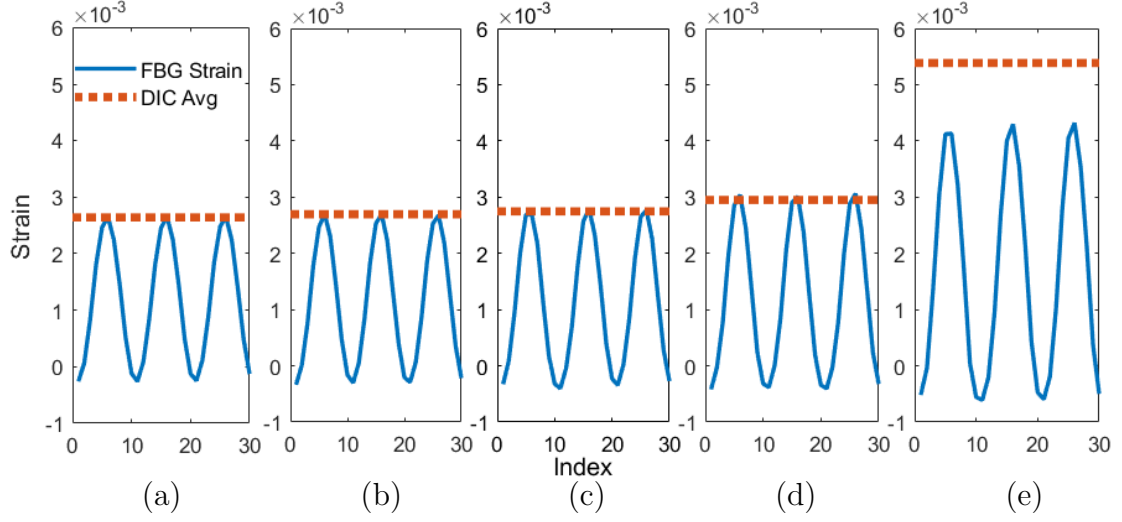


Figure 3.10: Comparison of the FBG strain signal and the average peak strain from DIC in the region of the FBG after (a) 2000, (b) 4000, (c) 6000, (d) 8000 and (e) 10000 cycles.

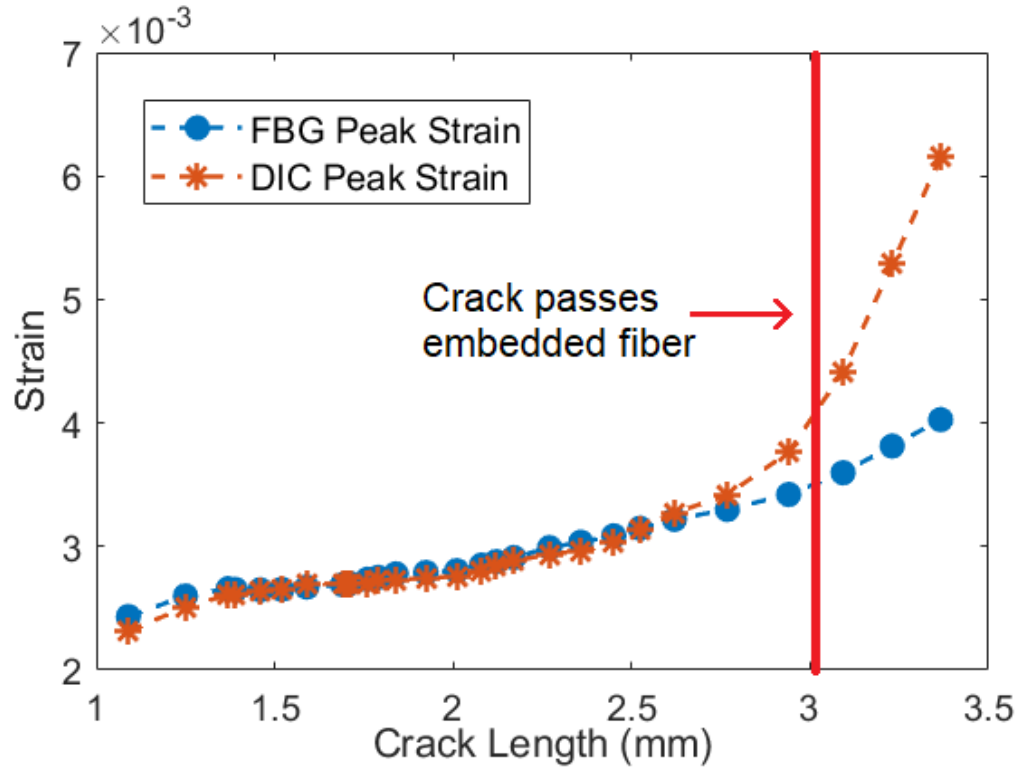


Figure 3.11: The FBG strain signal and the average peak strain from DIC in the region of the FBG as the crack length increased.

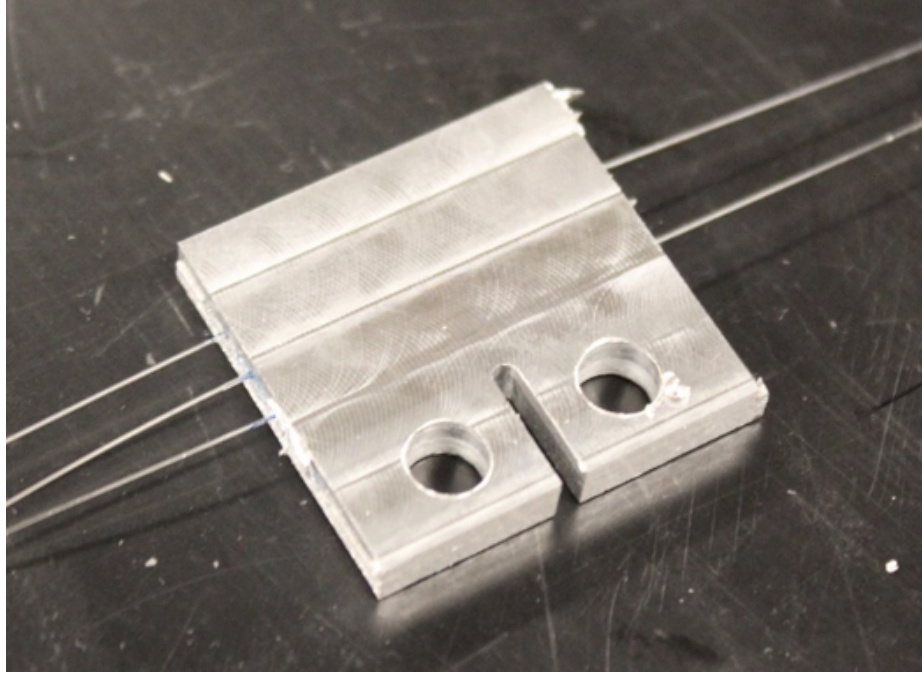


Figure 3.12: Compact tension (CT) specimen with three embedded FBG sensors built using UAM used in prognostic testing.

alternated between a higher amplitude regions to induce crack growth for 200 cycles and a lower amplitude region to test FBG sensing at smaller loads for 30 cycles. In the higher load regions, the tensile loads alternated between 200 N and 2 400 N and the low load regions, the tensile loads alternated between 200 N and 800 N. Once the crack had formed and began propagating the number of cycles at higher peak load was reduced to 30 cycles. Similar to the previous crack initiation testing, the wavelength at the peak loads was found before crack initiation had occurred. This was used to estimate the cycle where the expected peak signal exceed three standard deviations from the set means in both the high load and low load regions for all three embedded FBG sensors.

3.2.2 Results and Discussion

The prognostic analysis investigation utilized a CT specimen with three FBG sensors embedded at 3 mm, 6 mm and 9 mm from the notch as shown in Figure 3.12. There were two main alternating phases of the load profile with different goals. In the high amplitude, crack growth phase, the minimum crack length that can be detected was investigated. In the low amplitude phase, the signal with no crack was compared to when a crack was present but not quickly growing due to the low load. The signals from all three embedded FBG sensors were analyzed to compare how distance from the initiation site effected the results. The results from the test are show in Figure 3.13 and Figure 3.14. The 3 mm and 6 mm FBG signals are out of phase to the 9 mm FBG signal as force is not applied evenly to the CT specimen, which causes the side opposite the notch to be compressed when the load frame loads the coupon in tension.

During the test, the crack initiated and grew in a single cycle to a length of 0.350 mm. Using the analysis technique described in detail in Section 3.1, this increased crack length was detected by all three fibers in both the crack growth phase and the low amplitude phase. The following figures show the FBG signal as a solid line and the calculated upper bound of set means with no crack as a dotted line. The red circles indicate the mean of each set. When the red circle crosses above the dotted line, the FBG would have detected a crack. As Figures 3.15 - 3.20 illustrate, all embedded FBG sensors successfully detected the crack when it initiated to 0.350 mm after the seventh high amplitude set.

Although the signal change was less clear for FBG signals farther away from the notch, the fact that all three FBG sensors detected the crack growth illustrates the

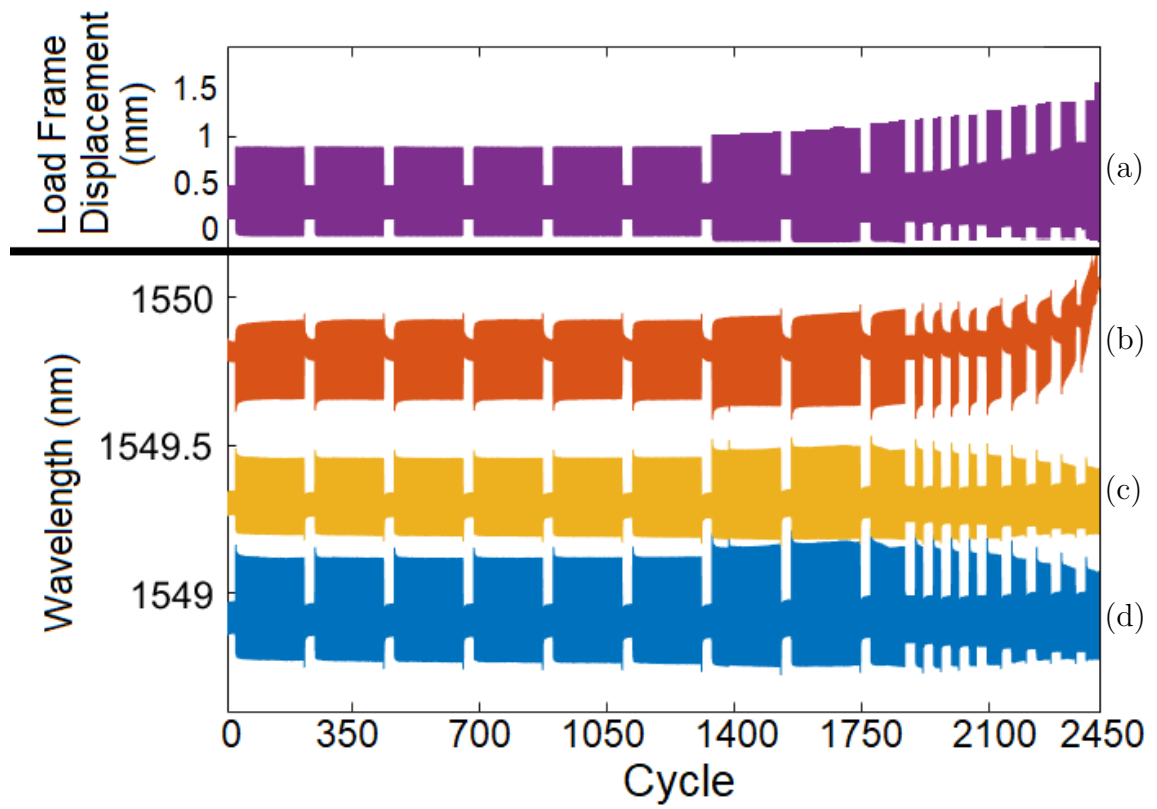


Figure 3.13: The load frame displacement (a) and the FBG signals from sensors embedded 9 mm (b), 6 mm (c) and 3 mm (d) from the notch over the entire prognostic analysis test.

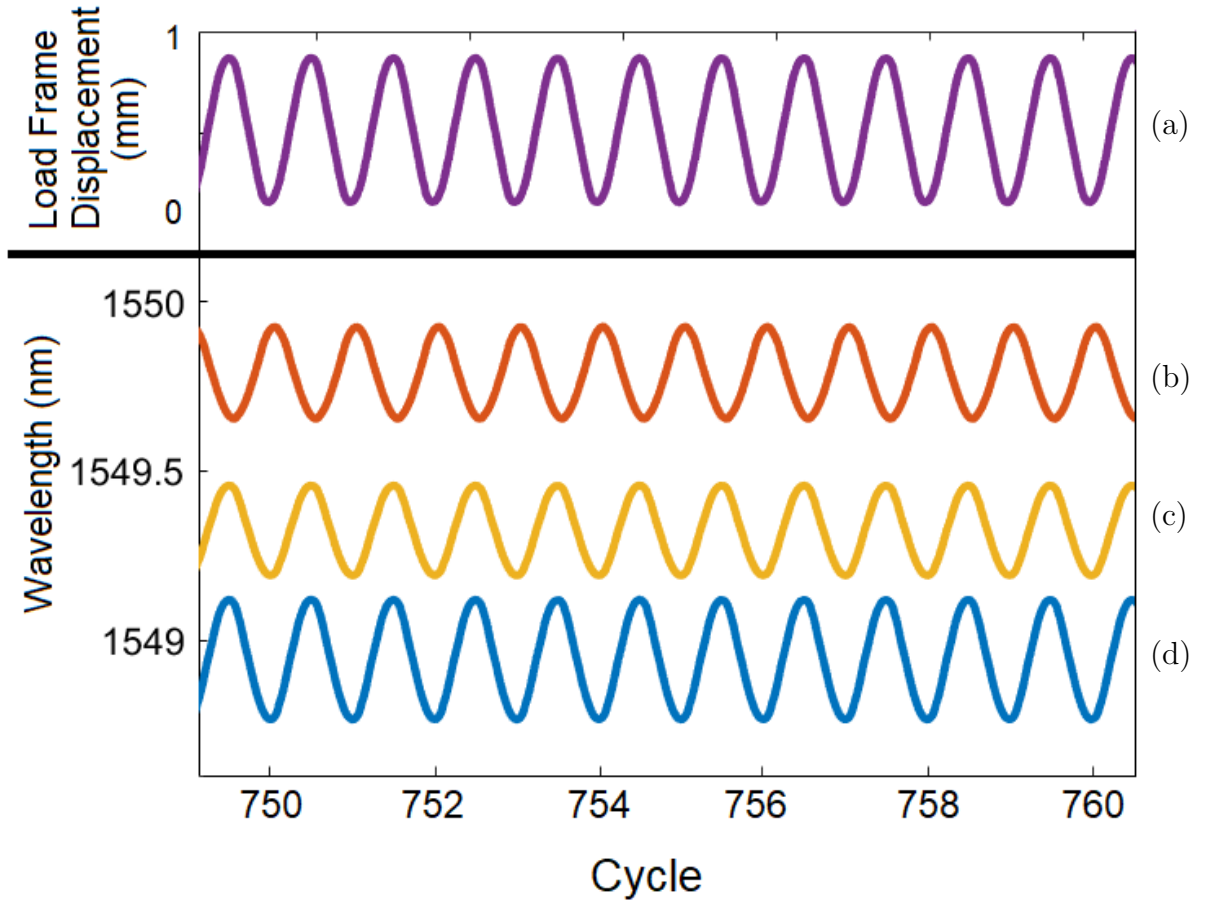


Figure 3.14: Detailed view of Figure 3.13 between cycles 749 to 761. Shown is the load frame displacement (a) and the FBG signals from sensors embedded 9 mm (b), 6 mm (c) and 3 mm (d) from the notch. Note the alternating crack growth phases with high strain and low amplitude phase with lower strain. The number of cycles of the crack growth phase was reduced toward the end of the test to ensure enough data was obtained as the crack grew.

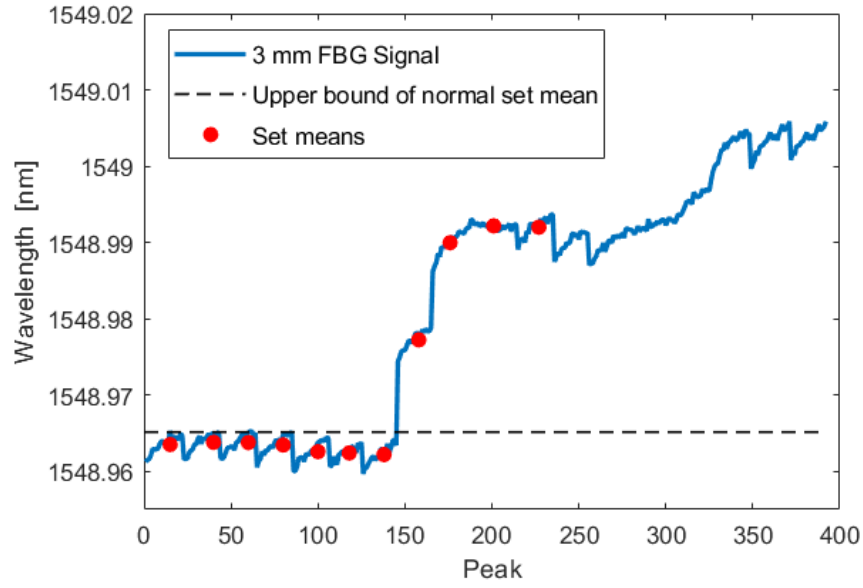


Figure 3.15: Crack detection analysis during low amplitude cyclic loading for embedded FBG 3 mm from notch tip. For this and subsequent images, the dashed line represents three standard deviations above the normal set mean.

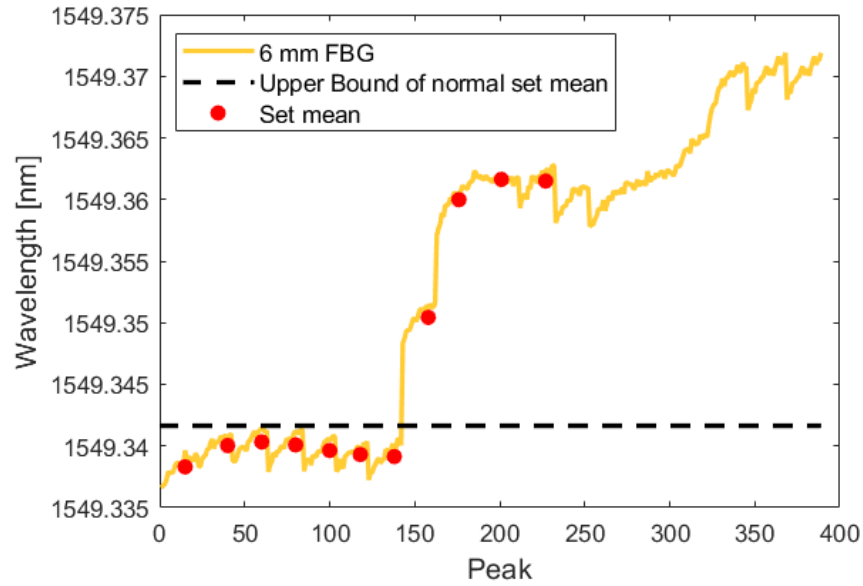


Figure 3.16: Crack detection analysis during low amplitude cyclic loading for embedded FBG 6 mm from notch tip.

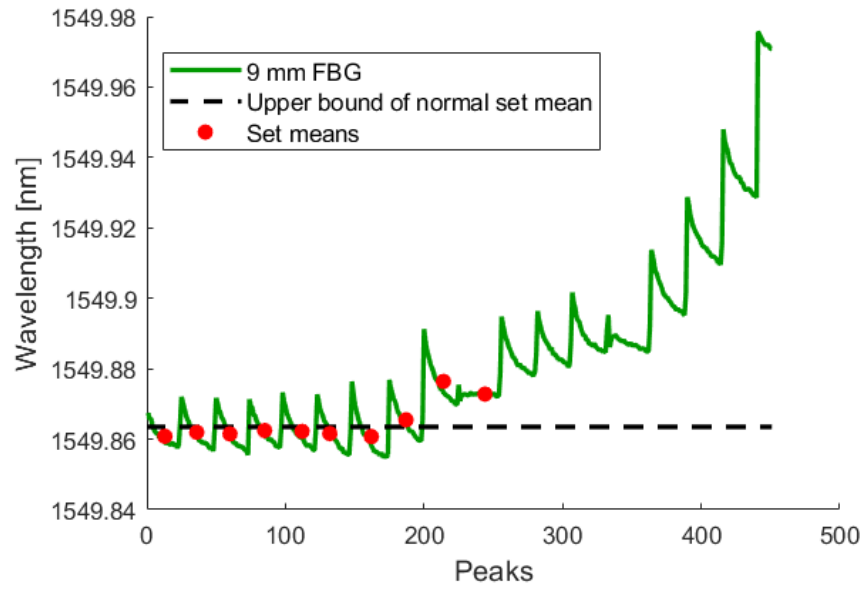


Figure 3.17: Crack detection analysis during low amplitude cyclic loading for embedded FBG 9 mm from notch tip.

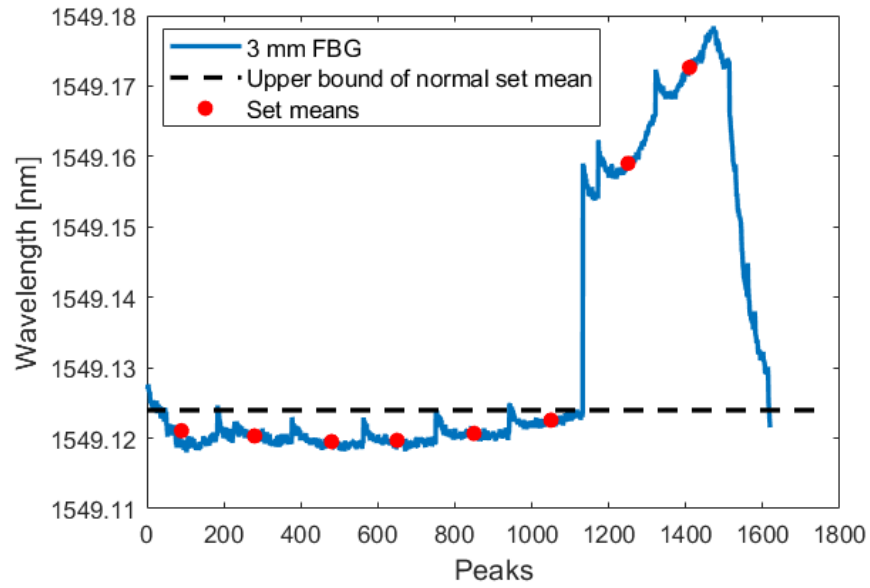


Figure 3.18: Crack detection analysis during high amplitude cyclic loading for embedded FBG 3 mm from notch tip.

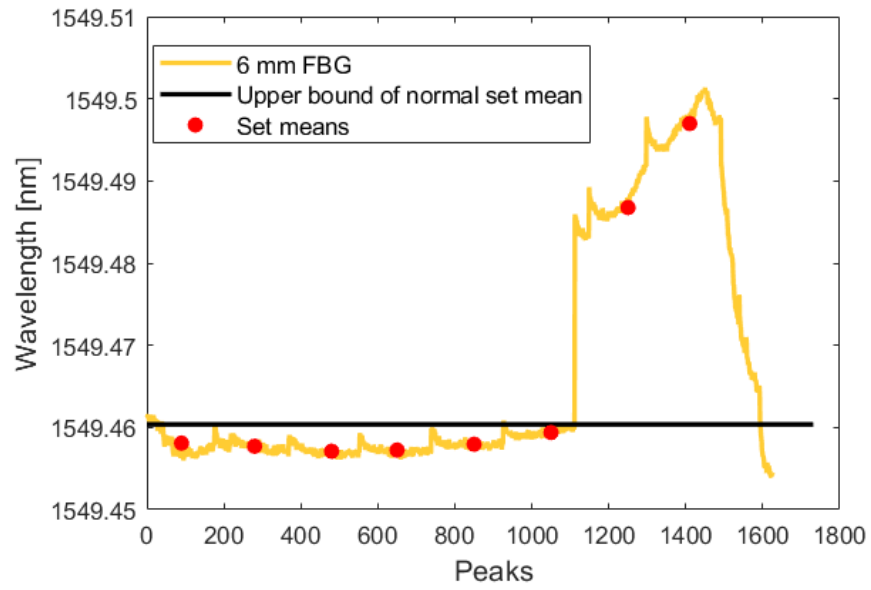


Figure 3.19: Crack detection analysis during high amplitude cyclic loading for embedded FBG 6 mm from notch tip.

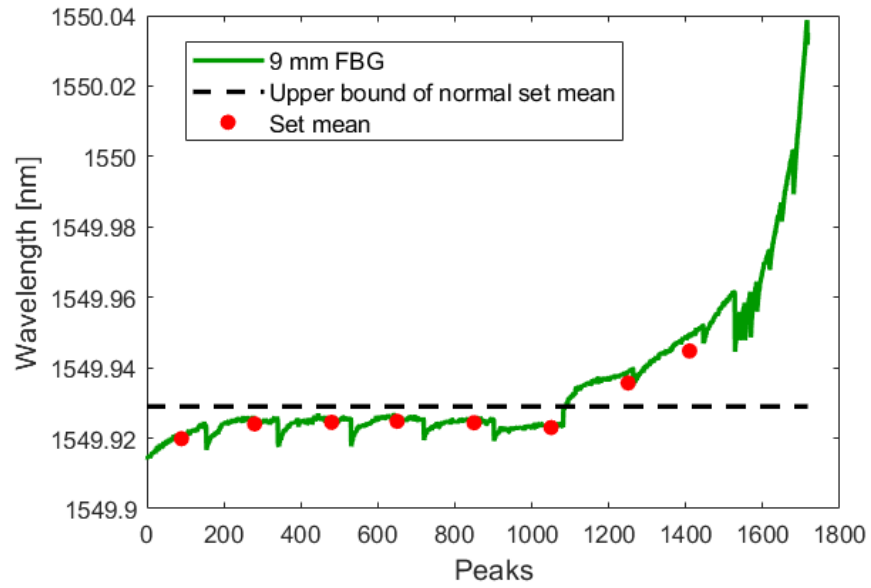


Figure 3.20: Crack detection analysis during high amplitude cyclic loading for embedded FBG 9 mm from notch tip.

potential robustness of UAM embedded FBG sensors in detecting crack initiation. Furthermore, the detection of the crack in the low amplitude phase, illustrates the ability of FBG sensors to detect minute defects even at normal operating conditions. Additional testing with more FBG sensors at more locations could provided deeper insight into the relationship between crack detection and embedded sensor locations.

3.3 Verification of Strain in CT Coupons

DIC and FEA were used to verify the strain values found by the embedded FBG sensors in CT specimen. In particular, the compression strain sensed by the FBG 9 mm from the crack tip was investigated.

While previous DIC testing used a narrow field of view to closely examine the crack tip, the DIC used in this test used a larger field of view encompassing the entire coupon with larger speckles on the coupon. The DIC analysis was only performed on a specimen without a crack for a few cycles to reduce the computational burden. The load profile ranged from 200 N to 2 000 N and followed a sine wave with a period of 0.25 Hz. The results of the DIC analysis at the maximum load of the cycle can be seen in Figure 3.21.

There are a number of features to discuss in Figure 3.21. As expected the highest strain is closest to the tip of the notch; however, the strain field varies throughout the entire CT specimen. In addition, the strain loosely follows vertical bands, which means the use of FBG sensors in CT specimens is justified as it is unlikely for the sensors to experience uneven strain resulting in multiple resonant peaks. This is validated by the experiments presented in Section 3.2 which did not exhibit any strain hopping characteristics. Furthermore, Figure 3.21 shows that the FBG embedded

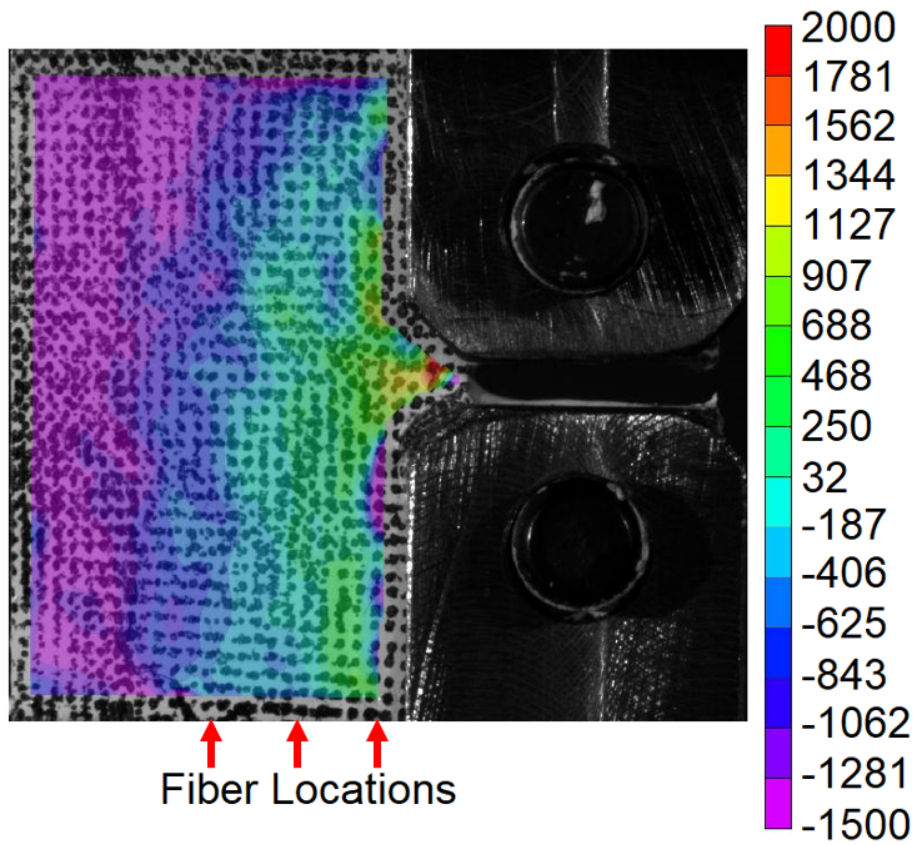


Figure 3.21: DIC of CT coupon with a load of 2000 N. Units of the legend are $\mu\epsilon$. The locations of embedded fibers at 3 mm, 6 mm and 9 mm are labeled.

9 mm from the notch tip experiences a compressive force, compared to the tensile force experienced by the 6 mm and 3 mm fibers. A neutral axis exists at approximately 7 mm. Future experiments could include an FBG embedded at this neutral axis to see how the sensing capabilities perform at this unique location. It is possible that a fiber embedded at this location would be more accurate at detecting damage if the variance during normal usage monitoring is smaller than in other regions.

FEA was also used to further examine the behavior of loaded CT specimens using Abaqus software by Dassault Systmes. A two dimension model of the CT coupon was created under the plane stress condition. The load was modeled by applying pressure on the upper edge of the top hole and lower edge of the bottom hole to model the clevis and pin system. The only boundary conditions were to restrict vertical displacement at the notch tip and the left boundary. The load and boundary conditions are presented in Figure 3.22.

No cyclic loading was done with FEA, instead the strain was examined at the peak load as was done with the embedded FBG sensors. This analysis was performed with a crack built into the sample of three different lengths: 0 mm, 0.35 mm, and 1.5 mm. In order to simulate a crack, elements at the front of the crack tip were removed in a straight line following the FEA procedure and results found in [61, 62, 63]. Cracks typically grow in a seemingly random and jagged manner, following grain boundaries and defects [64]. However, for the purposes of determining the strain field for FBG response, a slight variation in the direction of crack growth can be ignored.

Figure 3.23 presents the results of the FEA analysis. Similar to the DIC analysis, there are three main regions in the body of the CT specimen, an area of compression on the left side, an area of slight tension in the middle and an area of higher tension

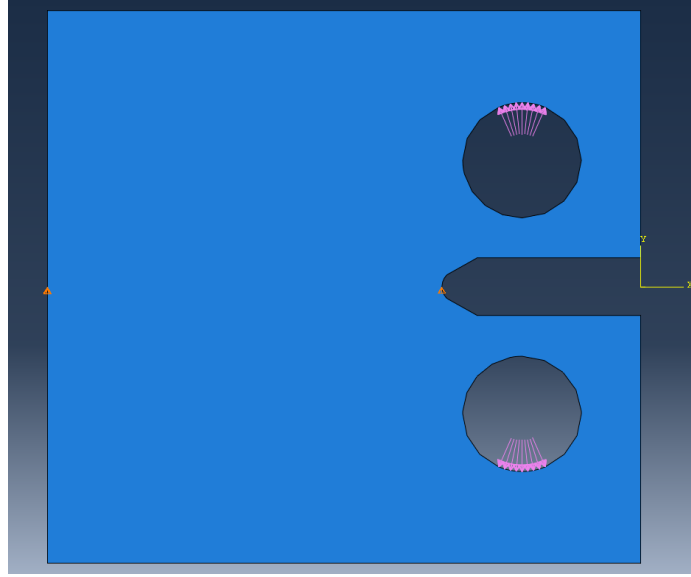
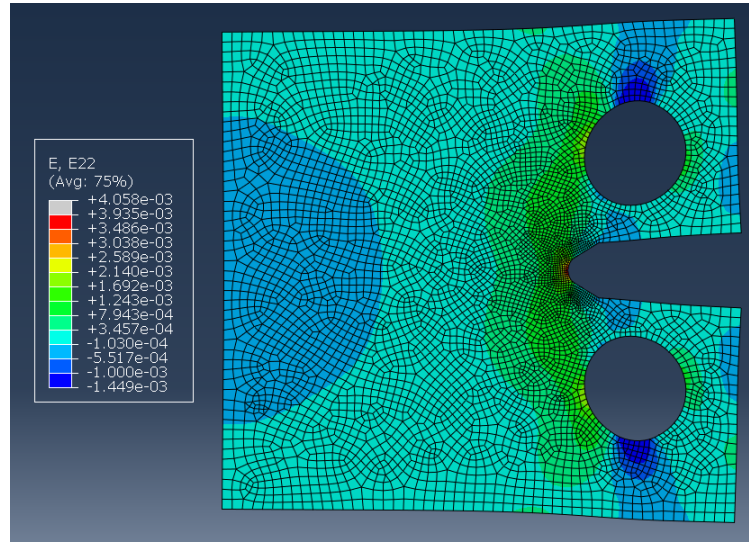
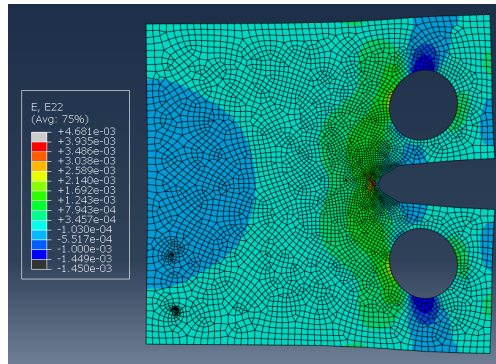


Figure 3.22: Location of loading and boundary conditions for FEA analysis.

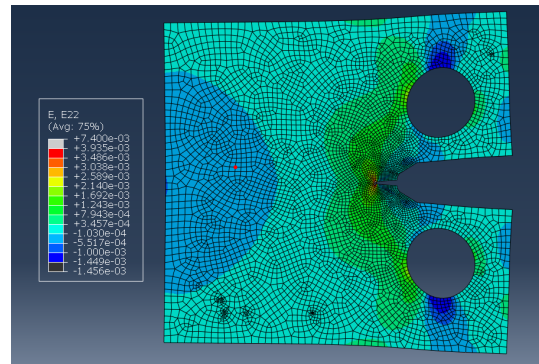
near the notch tip. This agrees with the prognostic analysis and DIC results. This analysis found the neutral axis to be about 7.2 mm from the notch tip. The magnitude of the strain at the locations of the embedded FBG sensors increases as the crack grows.



(a)



(b)



(c)

Figure 3.23: Results of Abaqus FEA analysis of CT specimen with (a) no crack, (b) a 0.35 mm crack, and (c) a 1.5 mm crack.

Chapter 4: Elevated Temperature Characterization

Many potential applications for SHM require sensors able to withstand elevated temperatures. A number of experiments were done in order to assess the feasibility of using UAM embedded FBG sensors in these applications. The outer coating of the optical fiber is the most susceptible to damage from elevated temperatures, and degradation was consequently examined through microscopy of cross sections. How the FBG signal behaves at elevated temperature was also investigated.

4.1 Static Temperature Testing of Embedded Fiber Optic Cable

Previous research has found that UAM embedded FBG sensors has demonstrated accurate strain sensing at temperatures significantly above the standard operating temperatures for short periods of time [33, 41, 59]. As the typical form of degradation of a fiber optic cable at elevated temperatures (starting at 80°C) is through the acrylate coating reacting with oxygen, the process of embedment should reduce the rate of reaction [59]. However, after the T6 heat treatment caused fiber degradation, further investigation was necessary to elucidate a deeper understanding of the effects of elevated temperatures on UAM embedded fibers optics.

4.1.1 Experimental Methods

This investigation was a pilot study into how temperature, time, and number of layers above the fiber impact the degradation of UAM embedded fiber optic cables. Two inch long coupons were made with an embedded fiber running longitudinally the entire length using the process outline in Section 1.4. Five tests were conducted each using three coupons that were visually inspected under a microscope to see if degradation had occurred. Each test was loosely based on the parameters of the T6 heat treatment.

The T6 heat treatment includes a step of 530°C for 45 minutes [65], which with only one layer above the fiber acted as a baseline. Three more tests each altered a single one of those variables, either temperature, time, or number of layers. A fifth test used the most favorable values of each variable. Additional test six and seven were performed on coupons where the fiber was fully encapsulated with no exit point to examine the effect of the presence of the exit point on degradation. In both tests without exit points, four layers were welded above the fibers to ensure no oxygen would be present. The oven was allowed to heat to the stable temperature, then the coupons were placed inside. After the conclusion of the test, the samples were removed and allowed to cool at room temperature. A summary of the test parameters can be seen in Table 4.1.

4.1.2 Results and Discussion

In Tests 1-5 with an exit point, the fibers showed significant degradation as demonstrated in the micrograph in Figure 4.1. Furthermore, the locations the fiber exited

Table 4.1: Summary of initial tests performed at elevated temperatures.

Test #	Comments	Temp. [°C]	Time [Minutes]	Welded Layers	Channel Exit
1	Control	530	45	1	Yes
2	Lower Temperature	400	45	1	Yes
3	Less Time	530	20	1	Yes
4	Additional layers	530	45	3	Yes
5	All parameters varied	350	20	4	Yes
6	No fiber exit and	400	20	4	No
7	all parameters varied	350	20	4	No

the coupons showed significant smoke stains (Figure B.12), which indicates the reaction was proceeding through the fiber exit points. Cross sections show that the degradation occurred throughout the entire fiber.

In Test 6 without fiber exit points, degradation occurred at 400°C for twenty minutes. Interestingly, bubbles formed during these tests where the expanding coating pushed into the layers welded above the fiber. In some cases, the bubble would leak and black (carbonized) coating would leak out. Images of these samples with bubbles can be seen in Figure 4.2. This result demonstrates that fiber degradation can occur even without the presence of oxygen.

On the other hand, the 350°C for twenty minutes Test 7 with no exit points did not result in degradation. Figure 4.3 shows a coupon after testing with no bubbles formed and a cross section micrograph showing an intact coating.

The results of this initial investigation provide valuable insight into the relationship between temperature, time, layers, and presence of channel exits on the degradation of embedded fibers. The only difference between Tests 5 and 7 was the presence of the fiber exit points. This result suggests that eliminating fiber exit points in

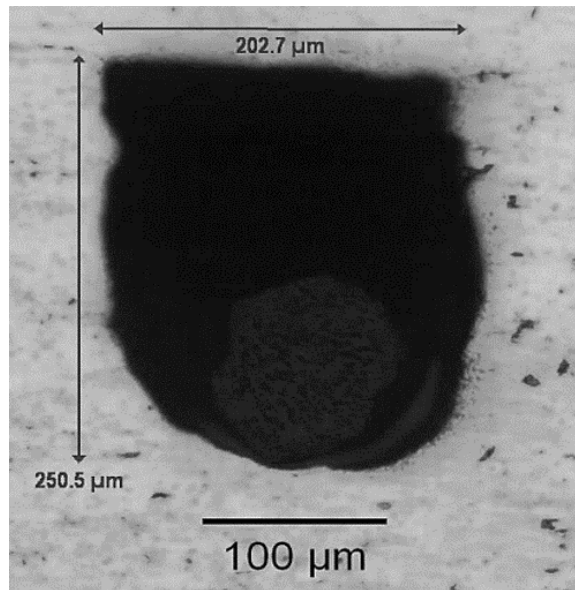


Figure 4.1: Cross section of coupon showing fiber degradation. Note the lack of clear internal fiber components.



Figure 4.2: Picture of coupons from Test 6 showing bubble formation.

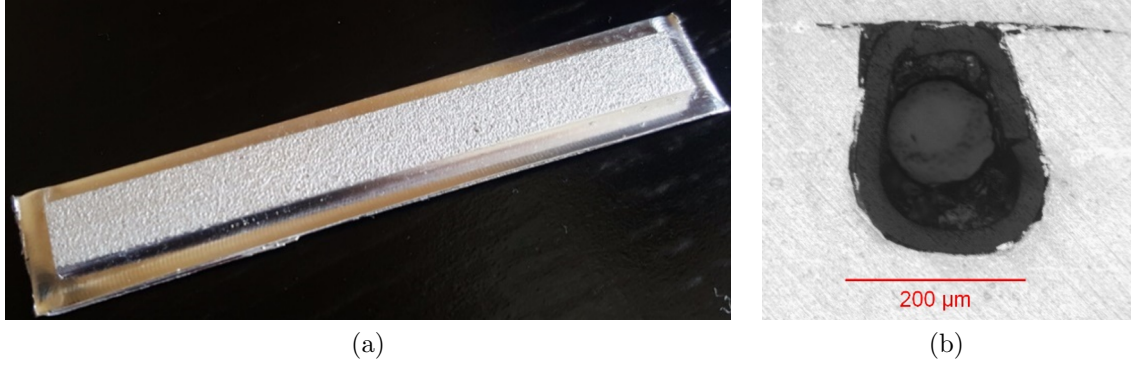


Figure 4.3: Example results from Test 7 showing (a) an intact coupon without any bubbles and (b) a cross section showing a fully intact fibers coating and structure.

elevated temperature regions will improve the fibers resistance to degradation. Comparing Tests 6 and 7 illustrates that a temperature boundary exists between 350°C and 400°C where degradation occurs even in without the presence of exit points. Additional cross sections are presented in Figure B.11. To greater establish the relationships between these variables, a complete design of experiments (DOE) could be performed in the future. However, spindle speed limitations in the CNC machine used for this thesis result in very long manufacturing times for channels. Consequently, manufacturing samples for a DOE would be extremely time consuming using this same machine.

4.2 Variable Temperature Testing With Embedded FBG

4.2.1 Experimental Methods

Two additional tests were designed to explore the main parameters that affect FBG signal at elevated temperatures. In the first test, the set point of the oven temperature was increased every thirty minutes until the FBG signal failed. Set

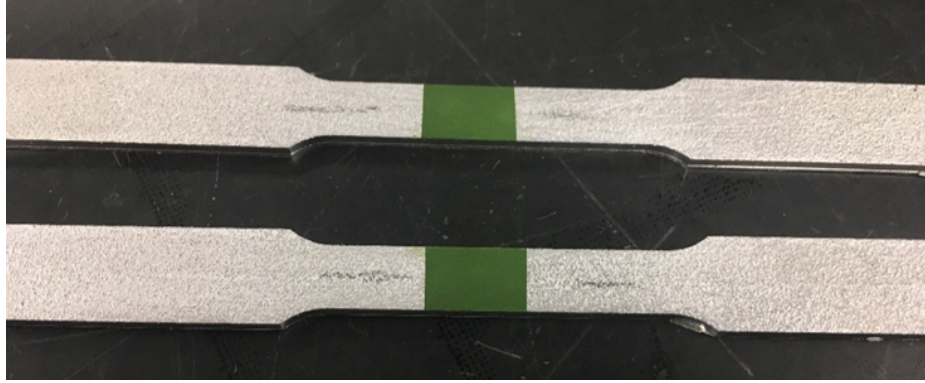


Figure 4.4: Elevated temperature coupons built using UAM with high temperature strain gauges affixed to the outside. FBG fibers are embedded down the length of each coupon.

points used were 50, 75, 100, 150, 200, 250, 300, 350, 400, 450°C. In the second test, a coupon was thermally cycled at increasing temperatures each cycle. The sample was placed in a cool oven and heated to a set temperature, then the oven was turned off until the temperature returned to room temperature. This was repeated at increasing temperature set points until FBG signal failure. Set points used were 50, 75, 100, 150, 200, 250, 300, 350°C. At the conclusion of the test, the sample was again heated to 350°C to test for permanent damage. Samples were then cross sectioned and micrographs were taken for optical evaluation.

Coupons were based on ASTM Standard E8: Standard Test Methods for Tension Testing of Metallic Materials with FBG sensors embedded in the middle of the sample [53]. A drawing of the coupon geometry is given in Figure A.1. The temperature was verified using a K-type thermocouple and the strain was verified using a high temperature strain gauge that was fixed with epoxy to the coupon as pictured in Figure 4.4.

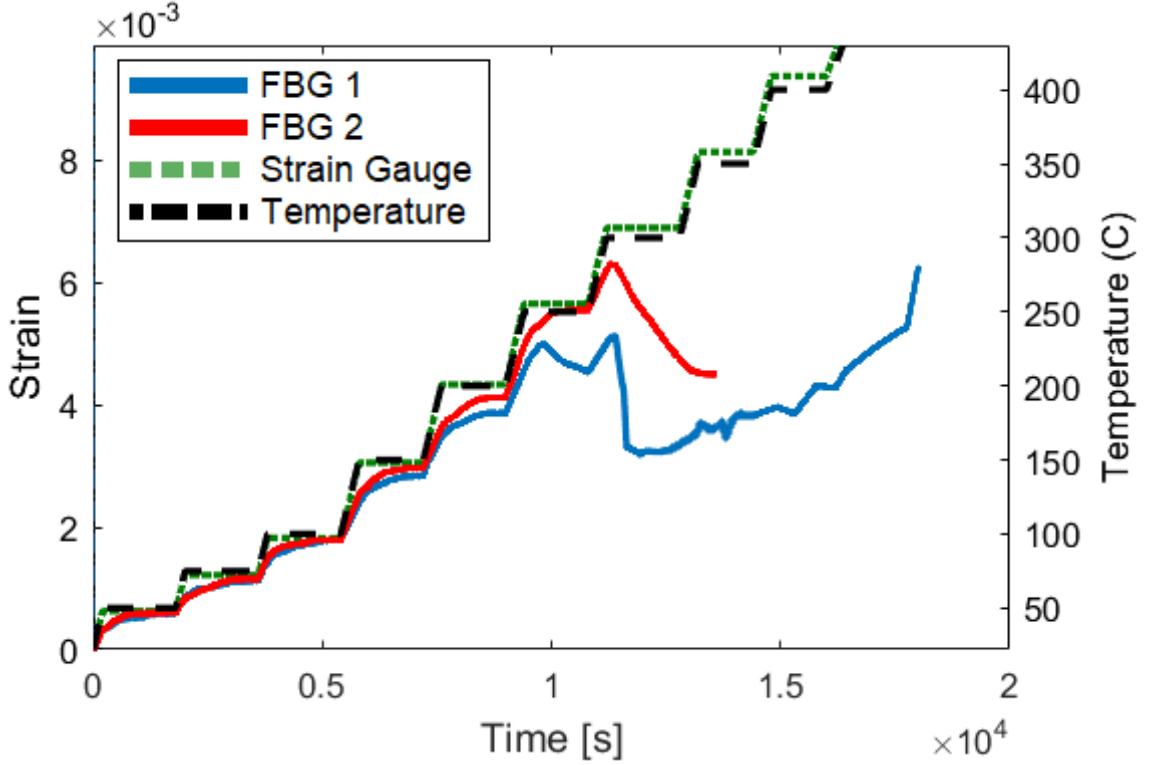


Figure 4.5: Elevated temperature testing of two UAM embedded FBG sensors. The strain measurements of two coupons with embedded FBG sensors and strain gauges is shown using the right axis. Using the left axis and shown in black is the temperature measurement from a thermocouple.

4.2.2 Results and Discussion

To continue to probe the effects of time and temperature on embedded fiber degradation, the test shown in Figure 4.5 was conducted. This test illustrated that FBG signal was able to accurately track the increasing temperature set points until between roughly 200 and 275°C. Note that this test does not independently test the effects of time and temperature, but rather focuses on the overall FBG signal.

Figure 4.6 shows a second elevated temperature test where a sample exhibited a repeatable signal up to 300°C. At the 350°C set point, there was a clear deviation

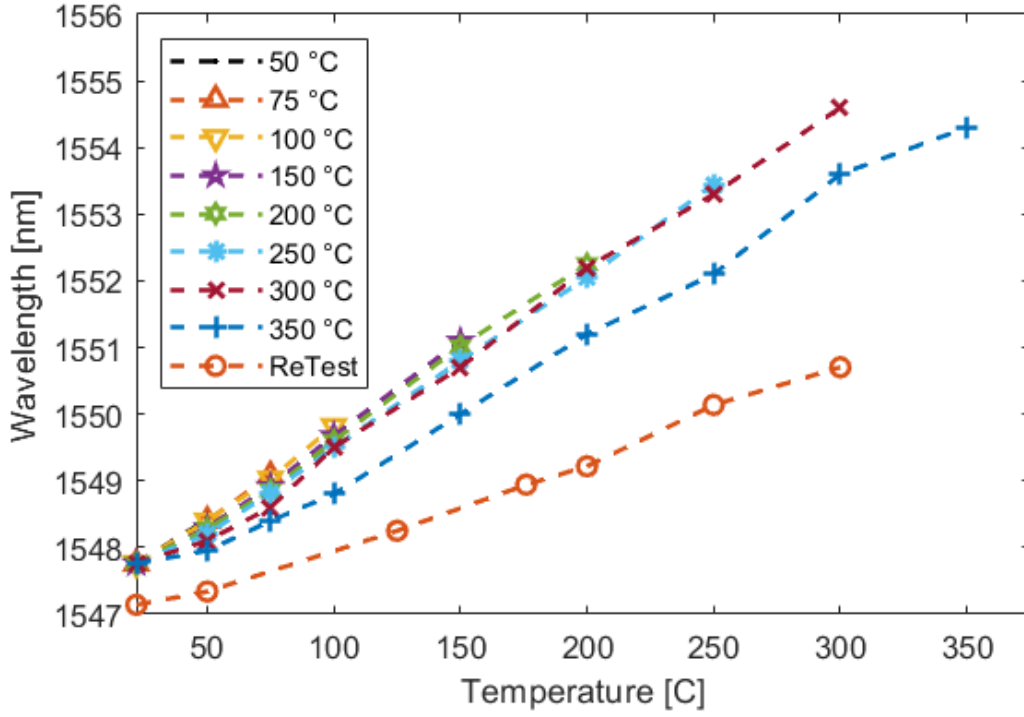


Figure 4.6: Elevated temperature cyclic testing of one UAM embedded FBG sensors. The FBG signal was measured during a cyclic temperature test with increasing oven set points. Once noticeable deviation occurred at 350°C, the test was performed one more time to see if permanent damage had occurred.

from the previous signal, and additional testing showed the signal was permanently affected. Again this test does not test any variables independently, and instead examines how the FBG signal behaves during thermal cycling.

The cross section of samples were then taken and examined through optical microscopy to identify any visible changes in structure. As seen in Figure 4.7, the control sample shows the clear and intact structures of the fiber: the outer coating, the inner coating, and the cladding (the core is not visible unless illuminated from behind). However, in the sample that had undergone elevated temperature testing, the outer

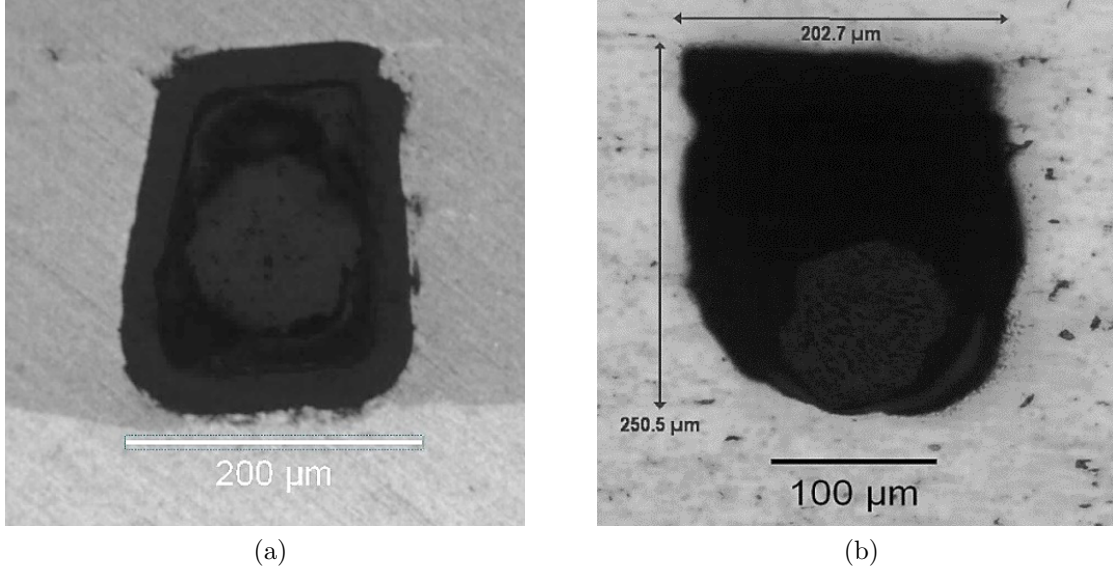


Figure 4.7: Comparison of the cross section of a UAM embedded FBG that has not undergone any thermal loading **(a)**, to the cross section of the embedded FBG from the cyclic testing **(b)**.

and inner coatings appear mostly gone and the cladding is no longer centered in the channel. This result was consistent across samples from both tests.

From these results, we conclude that by embedding FBG sensors into metal using UAM the operating temperature of the FBG increases. Both the temperature and time held at a elevated temperature appear to eventually lead to a degraded signal, although the exact relationship is still unknown and will require additional investigation.

Chapter 5: Conclusions and Future Prospects

Structural health monitoring (SHM) techniques are under utilized in many industries due to sensor limitations. With research into improved SHM techniques, new industries could unlock significant cost savings and improved safety. Fiber Bragg grating strain sensors that have been embedded into metal through Ultrasonic Additive Manufacturing (UAM) provide a promising candidate for emerging SHM applications. This thesis aimed to evaluate the prospect of using UAM embedded FBG sensors for SHM applications.

An important aspect of using embedded sensors is understanding the effect of the process on the mechanical characteristics of the material. Consequently, tensile and fatigue testing was performed on coupons with UAM embedded fiber optic cables. Due to the minimal cross-sectional area of the fiber, the embedment had very little effect on the tensile and fatigue properties of the coupons. Additional testing could help elucidate any minute differences in mechanical properties. In particular, it would be valuable to perform tensile and fatigue testing on various weight fractions of UAM builds with both H18 and T6 foils. Fatigue testing was generated using stress control; however, at the lower cycles to failure regions we were examining, strain control could provide results with less variability. Furthermore, because of the rectangular cross section of the coupons, a fully tensile cyclic test was performed. Although the

manufacturing time would be greater, it would be interesting to see how a UAM built coupon with a circular cross section would perform under tension-compression fatigue cycles. Finally, due to the difficulties in performing long tests, the endurance limit of the UAM samples was not found. This information would be particularly valuable for many industries as the lifetime of the sensor network is important.

This thesis also demonstrated the ability of UAM embedded FBG sensors to detect and track crack growth through the life of a CT specimen. Embedded FBG sensors were able to closely monitor crack growth until the crack passed the embedded fiber and the fiber began to slip. Embedded FBG sensors show promise for early crack detection, with sensors 3 mm from the crack initiation point detecting cracks with a length of only about 0.3 mm, an order of magnitude better than traditional NDI techniques. Even at distances of 6 mm and 9 mm, a crack was detected at 0.35 mm during both high load (crack growth phase) and low load (normal operating phase). This promising result demonstrates the potential for FBG sensors to act as prognostic tools during the operation of components. There is significant research still to be done before this technology can be implemented. A relationship between FBG sensor location and the size of crack at first detection is necessary to educate the location of embedment. Further FEA analysis could help facilitate this research. Another valuable experiment would be embedding FBG sensors in various components, perform usage monitoring during normal conditions and then introduce various defects to determine how the FBG signal changes. This process could involve attempting to determine the presence and extent of damage using only the FBG and load frame signals. Artificial intelligence could prove especially useful in these areas of prognostic research. Additional research is also necessary to discover the reason

for the decreasing peak wavelengths found during the first cycles whenever the peak load changed during testing.

Embedded FBG sensors were also shown to work at elevated temperatures, highlighting the possibility of higher temperature applications. A number of variables were identified to have an effect on fiber degradation: temperature, time, layers welded above the fiber and the presence of an exit point. To fully understand how each of the variables effects the degradation of fiber coating and the FBG signal an extended design of experiments could be used. It would be valuable to further understand the effects of the fiber exit points and potential ways to mitigate that effect, such as having the fiber exit away from the elevated temperature area, or coating the exits in an epoxy.

The process of embedding sensors into metal through UAM provides a novel technique for exploration with a variety of different sensors. Further research into different UAM embedded sensors would provide additional avenues of research for SHM applications and more. There is also room for additional FEA analysis of the embedment process and strain transfer to the fibers at both room and elevated temperatures. The challenge in these FEA studies is in determining the friction properties of the embedded fiber. Additional analysis and testing may be required to determine these values.

The work presented in this thesis lies at the distinctive intersection of structural health monitoring, ultrasonic additive manufacturing and fiber Bragg grating sensors. This unique location provides valuable insight into technology that could improve safety and decrease costs in the many industries that are underutilizing SHM systems.

Appendix A: Coupon Geometries

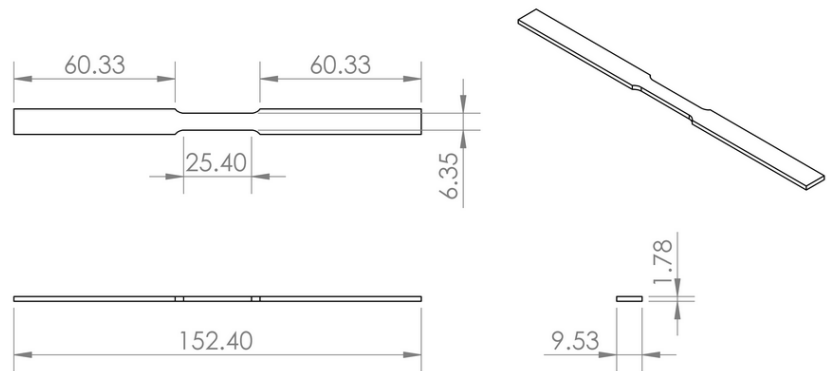


Figure A.1: Drawing of coupon used in the tensile testing and elevated temperature testing. Dimensions in mm. Based on designs from ASTM E8 [53].

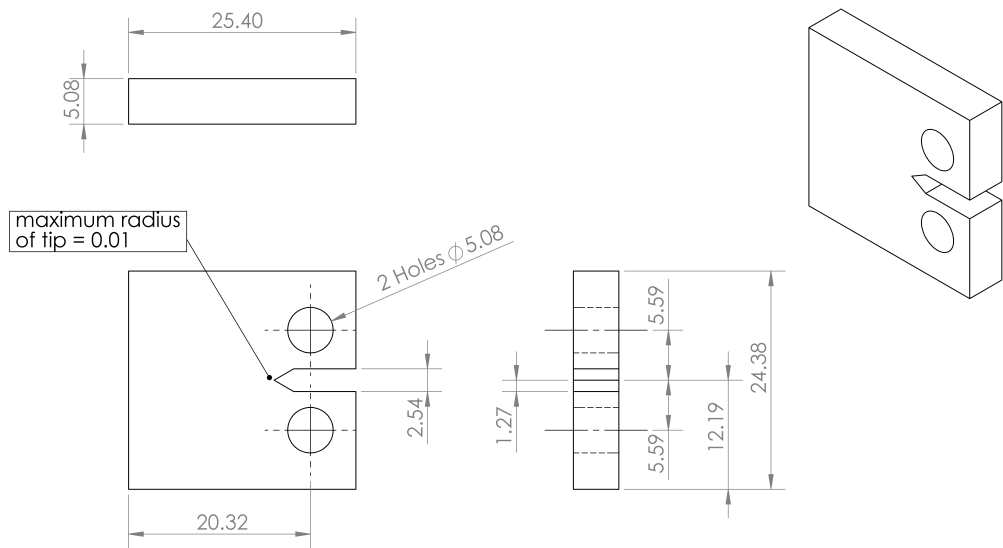


Figure A.2: Compact tension (CT) specimen geometry used in crack detection. All dimensions are in mm. Based on designs from ASTM E647 [58].

Appendix B: Additional Results and Considerations

B.1 Sensor Embedment Process

Additional images of the embedment process for a CT specimen with three FBG sensors are pictured in Figures B.1 - B.4.

B.2 Fatigue Testing

The original geometry of the fatigue samples included a curved channel with the fiber exit points not inside the grips of the load frames. During initial fatigue testing, this resulted in failures outside the gauge region that had to be discounted, as shown in Figure B.5. An updated geometry had the fibers exit inside the grip region, preventing these failures. .

B.3 Crack Growth

The DIC strain fields are shown in Figure B.6 for various images during the growth of a crack. For strain tracking of embedded FBG sensors, the FBG signal was calibrated to the predicted DIC strain. The DIC mean strain was calculated by averaging the strain in the region of the embedded fiber as shown in Figure B.7.

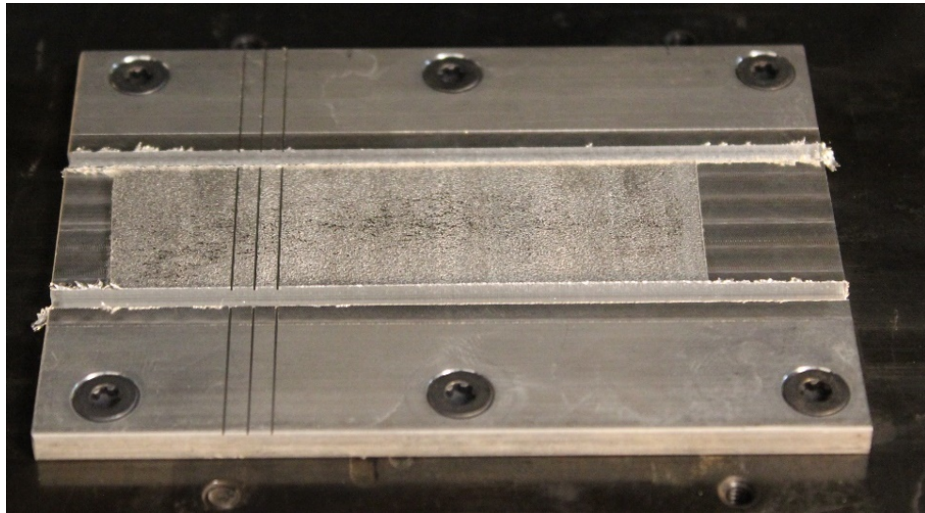


Figure B.1: After one layer welded by UAM, three channels are machined.

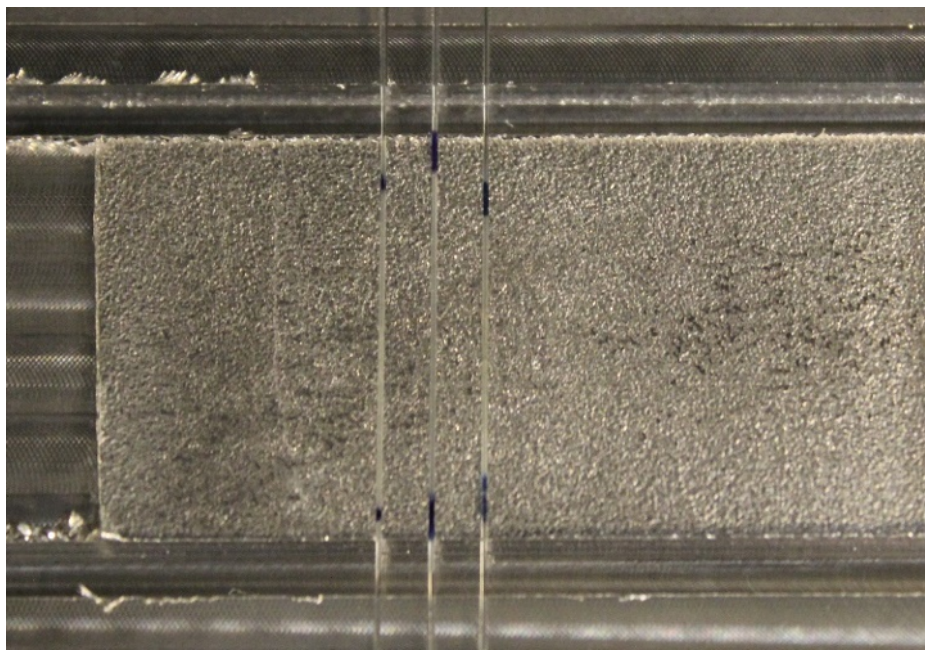


Figure B.2: The FBG sensors are then carefully placed in the channels.

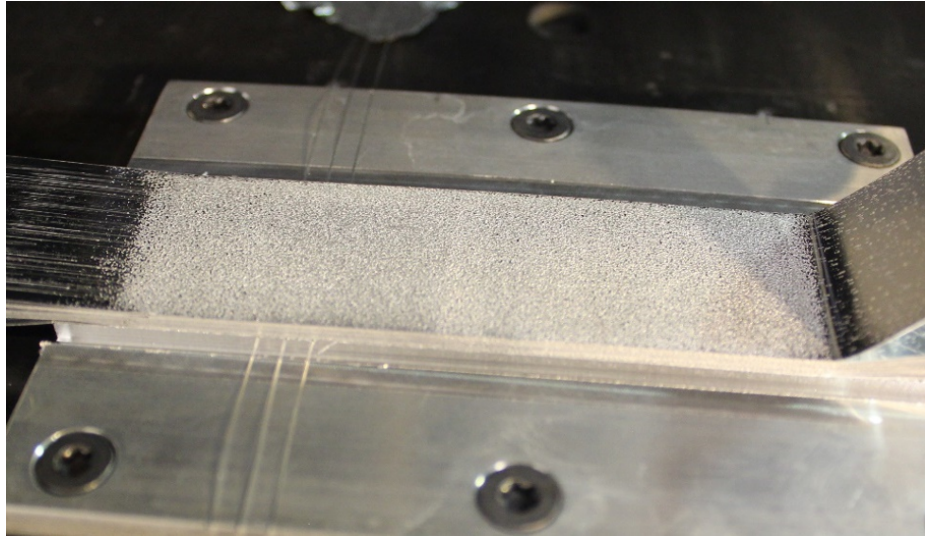


Figure B.3: Additional layers are then welded with UAM over the FBG sensors.

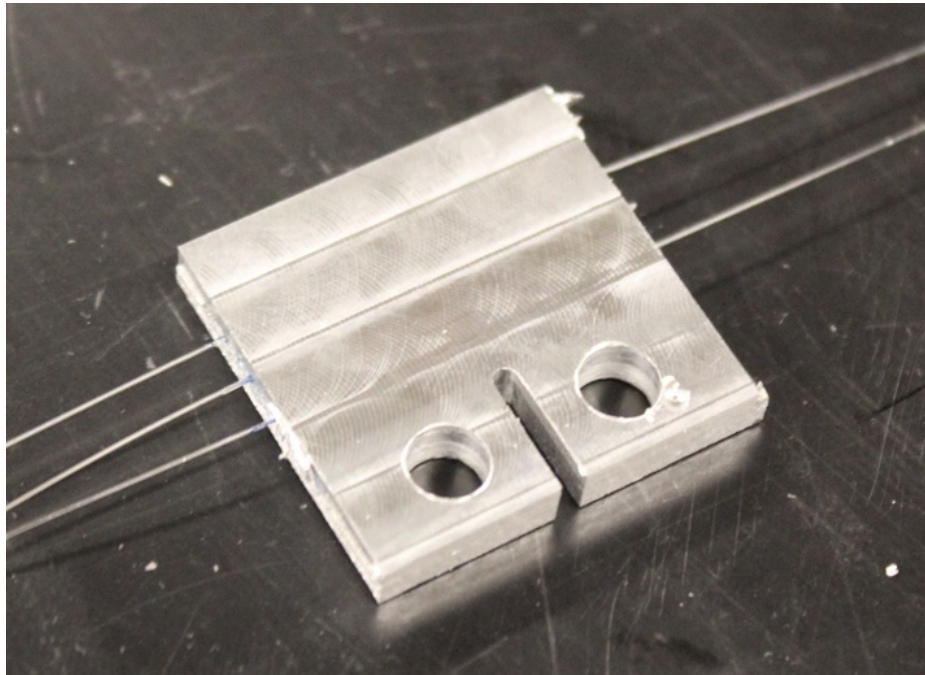


Figure B.4: A CNC machine mills out the final coupon geometry.

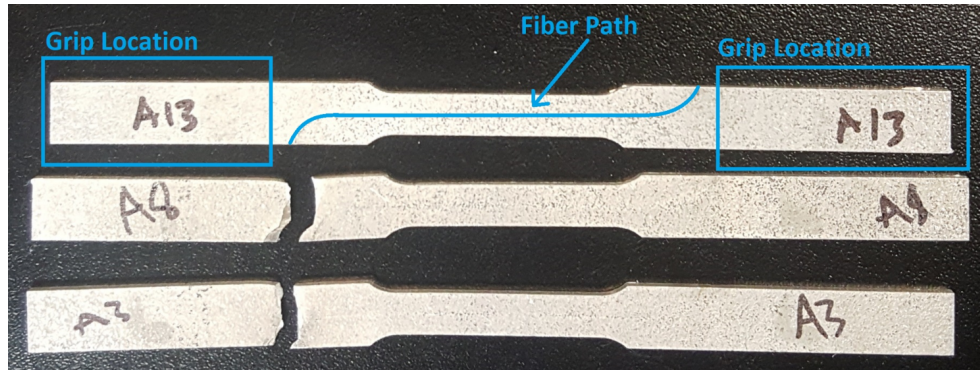


Figure B.5: Initial fatigue coupons failed outside the gauge region due to the fibers exiting coupons outside the grip region.

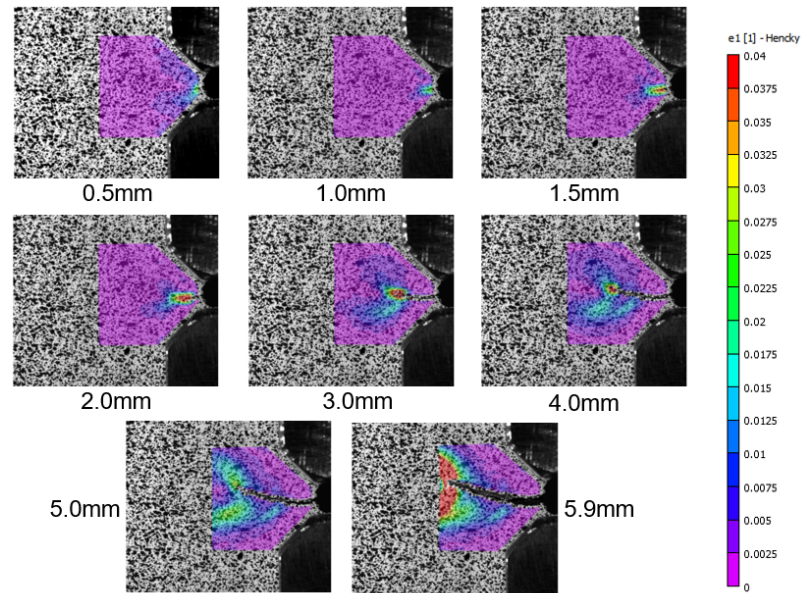


Figure B.6: DIC produced strain fields during the growth of a crack.

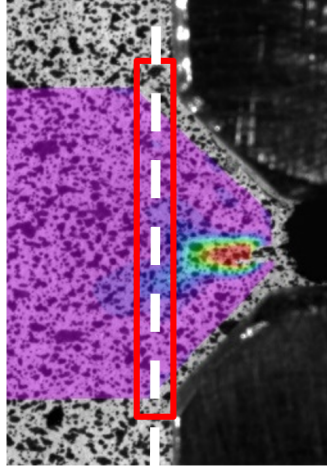


Figure B.7: To compare the FBG signal to the DIC strain, the DIC strain was averaged in the region of the fiber. The fiber is embedded at the white dotted line. The area of the strain field averaged in shown in the red box.

Next, as shown in Figure B.8, the ratio between the FBG voltage from the digital to analog converter was divided by the DIC mean strain in the fiber region to create an conversion factor between FBG voltage and strain. The early region of this ratio was then averaged and used to determine the FBG strain as the crack grew. This methodology allowed an accurate comparison between the two sensors to be made. This ratio also visualized how as the crack approached the fiber location, the FBG signal and DIC strain began to deviate.

The FBG signal was first able to detect a crack around the 195th cycle during the pre-cracking phase. An image of the CT specimen at cycle 195 is shown in Figure B.9 and a detailed image is shown in Figure B.10 where the 0.332 ± 0.046 mm crack is visible. The range of values comes from the fact that the crack entered a speckle and thus an exact end point could not be found.

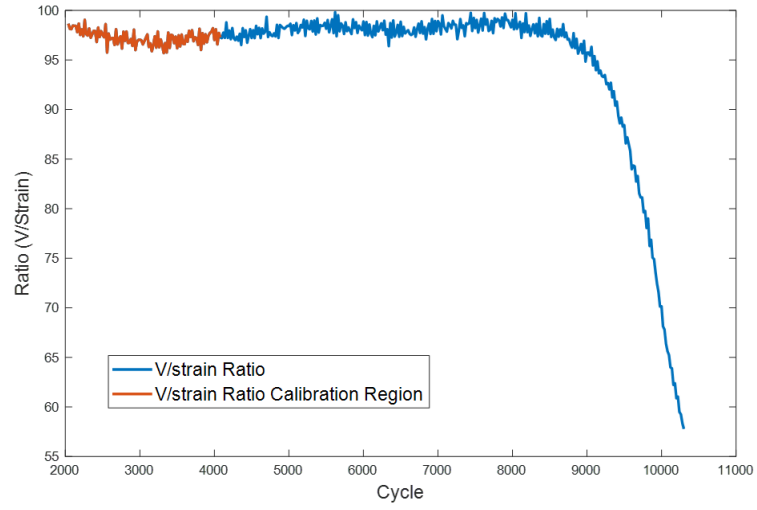


Figure B.8: The ratio between the voltage signal from the digital to analog converter and the DIC mean strain in the fiber region was found. The early region, shown in orange, was averaged and used to convert the FBG voltage signal to strain.

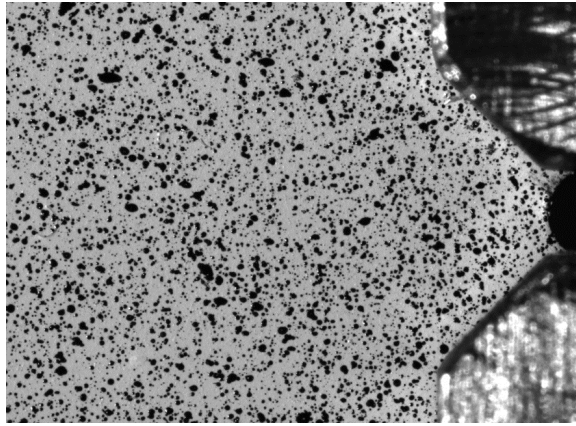


Figure B.9: The CT specimen at cycle 195 when the statistical analysis of the FBG signal first determined the presence of a crack.

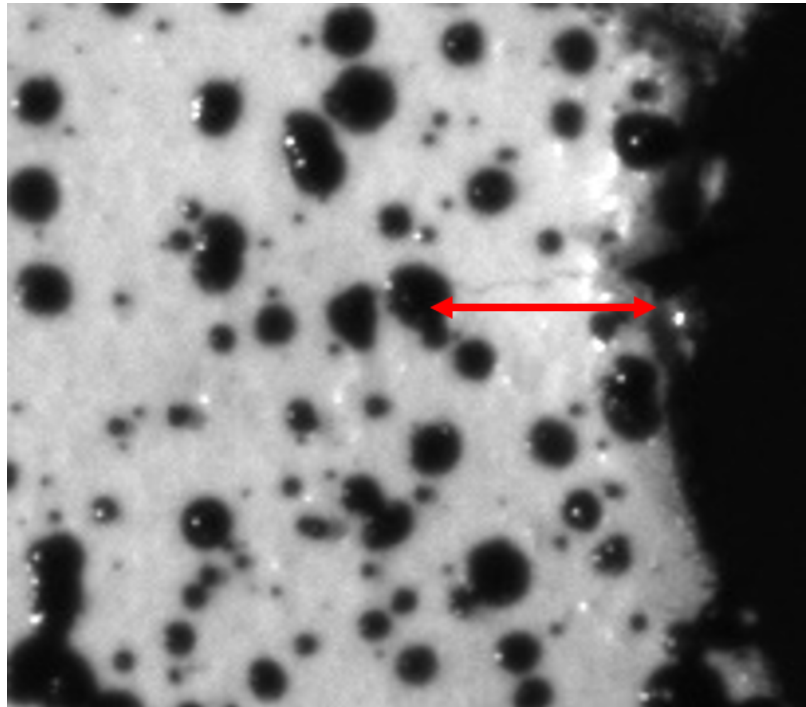


Figure B.10: Detailed view of Figure B.9. The red arrow shows the location and length of the crack. Note how the crack enters a speckle, so the exact end point cannot be determined. Each pixel of the photograph corresponds to 0.0054 mm.

B.4 Elevated Temperature

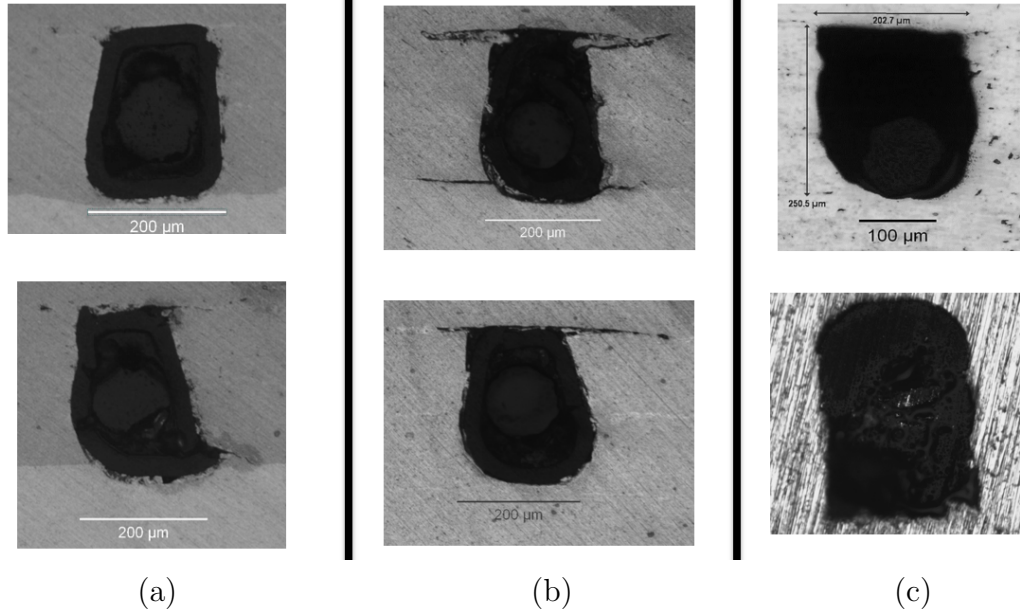


Figure B.11: Additional cross-sections of coupons that have undergone elevated temperature testing; (a) control with no elevated temperature testing; (b) coupons tested at 350°C for 20 minutes; (c) coupons tested at 400°C for 20 minutes. Note that both (a) and (b) show no damage to fiber structure (cracks in (b) are likely due to insufficient channel depth). On the other hand, (c) shows cross-sections with clearly damaged fibers and signs of remelting of the acrylate.

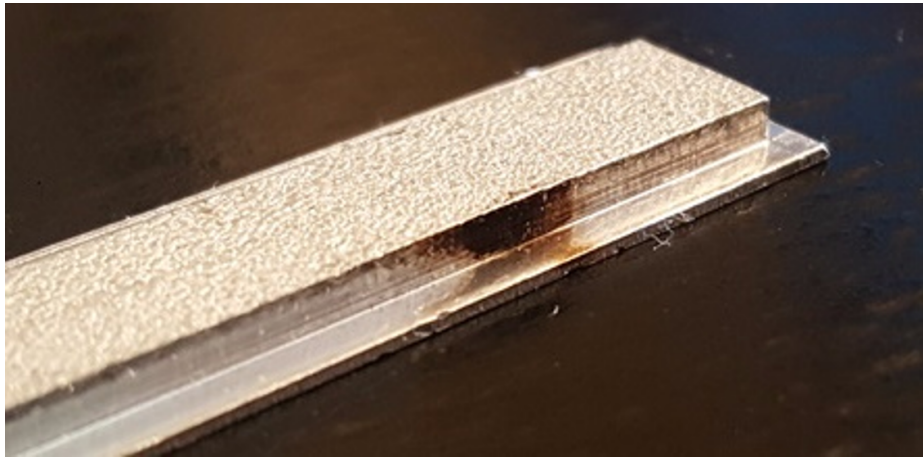


Figure B.12: Example of smoke stains at the fiber exit point of the coupon.

Bibliography

- [1] H. Sohn, C.R. Farrar, F.M. Hemez, and J.J. Czarnecki, “A review of structural health monitoring literature: 1996-2001,” 2004.
- [2] M.A.b. Abdo, *Structural health monitoring history, applications and future*. Open Science Publishers, 2014.
- [3] C.R. Farrar and K. Worden, “An introduction to structural health monitoring,” *Philosophical Transactions of The Royal Society A*, 365, 303–315, 2007.
- [4] S. Taheri, “A review on five key sensors for monitoring of concrete structures,” *Construction and Building Materials*, 204, 492–509, 2019.
- [5] A.A. Khan, S. Zafar, N.S. Khan, and Z. Mehmood, “History, current status and challenges to structural health monitoring system aviation field,” *Journal of Space Technology*, 4, 1–8, 2014.
- [6] T. Dong and N.H. Kim, “Cost-effectiveness of structural health monitoring in fuselage maintenance of the civil aciation industry,” *Aerospace*, 5, (3), 2018.
- [7] M. Fioriti, “Impacts of a prognostic and health management system on aircraft fleet operating cost during conceptual design phase by using parametric estimation,” *Challengesin European Aerospace*, 2015.
- [8] M. Gerdes, D. Galar, and D. Scholz, “Effects of condition-based maintenance on costs caused by unscheduled maintenance of aircraft,” *Journal of Quality in Maintenance Engineering*, 22, (4), 394–417, 2016.
- [9] S. Kessler, S. Spearing, and C. Soutis, “Damage detection in composite materials using Lamb wave methods,” *Smart Materials and Structures*, 11, (2), 2002.
- [10] Z. Wu, M.J. Dapino, and S.K. Chilelli, “Convolutional neural network for metallic fracture detection using digital image correlation,” *Sensors*, 2019.
- [11] S. Das and P. Saha, “A review of some advanced sensors used for health diagnosis of civil engineering structures,” *Measurement: Journal of the International Measurement Confederation*, 129, 68–90, 2018.

- [12] S. Sony, S. Laventure, and A. Sadhu, “A literature review of next-generation smart sensing technology in structural health monitoring,” *Structural Control and Health Monitoring*, 26, (3), 1–22, 2019.
- [13] M. Majumder, T.K. Gangopadhyay, A.K. Chakraborty, K. Dasgupta, and D.K. Bhattacharya, “Fibre Bragg gratings in structural health monitoring-Present status and applications,” *Sensors and Actuators, A: Physical*, 147, (1), 150–164, 2008.
- [14] T.J. Arsenault, A. Achuthan, P. Marzocca, C. Grappasonni, and G. Coppotelli, “Development of a FBG based distributed strain sensor system for wind turbine structural health monitoring,” *Smart Materials and Structures*, 22, (7), 2013.
- [15] A.A. Stolov, J.A. Wrubel, and D.A. Simoff, “Thermal stability of specialty optical fiber coatings,” *Journal of Thermal Analysis and Calorimetry*, 124, (3), 1411–1423, 2016.
- [16] K. Worden and E.J. Cross, “On switching response surface models, with applications to the structural health monitoring of bridges,” *Mechanical Systems and Signal Processing*, 98, 139–156, 2018.
- [17] H. Murayama, K. Kageyama, H. Naruse, A. Shimada, and K. Uzawa, “Application of fiber optic distributed sensors to health monitoring for full-scale composite structures,” *Journal of Intelligent Material Systems and Structures*, 2003.
- [18] M. Werneck, R.C.S.B. Allil, B.A. Ribeiro, and F.V.B. de Nazare, “A guide to fiber Bragg grating sensors,” in *Current Trends in Short and Long Period Fiber Gratings*, Ch. 1, IntechOpen, 2013.
- [19] H. Hadjiantonis, “Bragg’s law,” Accessed at: https://commons.wikimedia.org/wiki/File:Bragg%27s_law.svg, 2013.
- [20] K.O. Hill and G. Meltz, “Fibber Bragg grating technology fundamentals and overview,” *Journal of Lightwave Technology*, 15, (8), 1263–1276, 1997.
- [21] M. Kreuzer, “Strain measurement with fiber bragg grating sensors,” HMB GmbH, 2006.
- [22] R.J. Black, D. Zare, L. Oblea, Y.L. Park, B. Moslehi, and C. Neslen, “On the gage factor for optical fiber grating strain gages,” *Proceedings of Society for the Advancement of Materials and Process Engineering (SAMPE’08)*, 52, 2008.
- [23] A. Othonos, K. Kalli, D. Pureur, and A. Mugnier, “Fibre Bragg gratings,” in *Wavelength Filters in Fibre Optics* (H. Venghaus, ed.), Ch. 5, 189–269, Berlin: Springer, 2nd ed., 2006.

- [24] J. Zhou, Z. Zhou, and D. Zhang, “Study on strain transfer characteristics of fiber Bragg grating sensors,” *Journal of Intelligent Material Systems and Structures*, 21, (11), 1117–1122, 2010.
- [25] D. Havermann, J. Mathew, W.N. Macpherson, R.R.J. Maier, and D.P. Hand, “In-situ strain sensing with fiber optic sensors embedded into stainless steel 316,” *Sensors and Smart Structures Technologies for Civil, Mechanical, and Aerospace Systems 2015*, 9435, 2015.
- [26] D. Havermann, J. Mathew, W.N. MacPherson, D.P. Hand, and R.R.J. Maier, “Measuring residual stresses in metallic components manufactured with fibre Bragg gratings embedded by selective laser melting,” *24th International Conference on Optical Fibre Sensors*, 9634, 2015.
- [27] T. Grandal, S. Fraga, G. Castro, E. Vazquez, and A. Zornoza, “Laser cladding-based metallic embedding technique for fiber optic sensors,” *Journal of Lightwave Technology*, 36, (4), 1018–1025, 2018.
- [28] R.R.J. Maier, D. Havermann, O. Schneller, J. Mathew, D. Polyzos, W.N. MacPherson, and D.P. Hand, “Optical fibre sensing in metals by embedment in 3D printed metallic structures,” *23rd International Conference on Optical Fibre Sensors*, 9157, (07), 2014.
- [29] J. Mathew, C. Hauser, P. Stoll, C. Kenel, D. Polyzos, D. Havermann, W.N. Macpherson, D.P. Hand, C. Leinenbach, A. Spierings, K. Koenig-Urban, and R.R. Maier, “Integrating fiber fabry-perot cavity sensor into 3-D printed metal components for extreme high-temperature monitoring applications,” *IEEE Sensors Journal*, 17, (13), 4107–4114, 2017.
- [30] K. Graff, “Ultrasonic additive manufacturing,” in *Welding Fundamentals and Processes* (T. Lienert, T. Siewert, S. Babu, and V. Acoff, eds.), 731–741, ASM International, 2011.
- [31] P. Wolcott and M. Dapino, “Ultrasonic additive manufacturing,” in *3D Printing Handbook: Product Development for the Defense Industry*, Ch. 17, 275–313, CRC Press, badiru, a. ed., 2017.
- [32] A. Hehr and M.J. Dapino, “Dynamics of ultrasonic additive manufacturing,” *Ultrasonics*, 73, 49–66, 2017.
- [33] J.J. Schomer, *Embedding fiber Bragg grating sensors through ultrasonic additive manufacturing*. PhD thesis, The Ohio State University, 2017.

- [34] A. Levy, A. Miriyev, N. Sridharan, T. Han, E. Tuval, S.S. Babu, M.J. Dapino, and N. Frage, “Ultrasonic additive manufacturing of steel: method, post-processing treatments, and properties,” *Journal of Materials Processing Technology*, 256, 183–189, 2018.
- [35] P.J. Wolcott, N. Sridharan, S.S. Babu, A. Miriyev, N. Frage, and M.J. Dapino, “Characterisation of AlTi dissimilar material joints fabricated using ultrasonic additive manufacturing,” *Science and Technology of Welding and Joining*, 21, (2), 114–123, 2016.
- [36] H. Guo, M.B. Gingerich, L.M. Headings, R. Hahnlen, and M.J. Dapino, “Joining of carbon fiber and aluminum using ultrasonic additive manufacturing (UAM),” *Composite Structures*, 208, 180–188, 2019.
- [37] X. Chen, A. Hehr, M.J. Dapino, and P.M. Anderson, “Deformation mechanisms in NiTi-Al composites fabricated by ultrasonic additive manufacturing,” *Shape Memory and Superelasticity*, 1, (3), 294–309, 2015.
- [38] A. Bournias-Varotsis, R.J. Friel, R.A. Harris, and D.S. Engstrøm, “Ultrasonic Additive Manufacturing as a form-then-bond process for embedding electronic circuitry into a metal matrix,” *Journal of Manufacturing Processes*, 32, 664–675, 2018.
- [39] S. Masurtschak, R.J. Friel, and R.A. Harris, “New concept to aid efficient fibre integration into metal matrices during ultrasonic consolidation,” *Proceedings of the Institution of Mechanical Engineers, Part B: Journal of Engineering Manufacture*, 231, (7), 1105–1115, 2017.
- [40] T. Monaghan, A.J. Capel, S.D. Christie, R.A. Harris, and R.J. Friel, “Solid-state additive manufacturing for metallized optical fiber integration,” *Composites Part A: Applied Science and Manufacturing*, 76, 181–193, 2015.
- [41] J.J. Schomer, A.J. Hehr, and M.J. Dapino, “Characterization of embedded fiber optic strain sensors into metallic structures via ultrasonic additive manufacturing,” *Sensors and Smart Structures Technologies for Civil, Mechanical, and Aerospace Systems 2016*, 9803, 980320, 2016.
- [42] A. Hehr, M. Norfolk, J. Wenning, J. Sheridan, P. Leser, P. Leser, and J.A. Newman, “Integrating fiber optic strain sensors into metal using ultrasonic additive manufacturing,” *JOM*, 70, (3), 315–321, 2018.
- [43] C. Mou, P. Saffari, D. Li, K. Zhou, L. Zhang, R. Soar, and I. Bennion, “Smart structure sensors based on embedded fibre Bragg grating arrays in aluminium alloy matrix by ultrasonic consolidation,” *Measurement Science and Technology*, 20, (3), 1–6, 2009.

- [44] A. Hehr and M.J. Dapino, “Interfacial shear strength estimates of NiTi-Al matrix composites fabricated via ultrasonic additive manufacturing,” *Composites Part B: Engineering*, 77, 199–208, 2015.
- [45] C.D. Hopkins, P.J. Wolcott, M.J. Dapino, A.G. Truog, S.S. Babu, and S.A. Fernandez, “Optimizing ultrasonic additive manufactured Al 3003 properties with statistical modeling,” *Journal of Engineering Materials and Technology*, 134, (1), 2012.
- [46] R. Dehoff and S. Babu, “Characterization of interfacial microstructures in 3003 aluminum alloy blocks fabricated by ultrasonic additive manufacturing,” *Acta Materialia*, 58, (13), 4305–4315, 2010.
- [47] K. Graff, J. Devine, J. Keltos, and N. Zhou, “Ultrasonic welding of metals,” in *American Welding Society Welding Handbook*, American Welding Society, 2000.
- [48] I. Inagaki, T. Takechi, Y. Shirai, and N. Ariyasu, “Application and Features of titanium for the aerospace industry,” Nippon Steel & Sumitomo Metal, 2014.
- [49] A.E. Wilson-Heid, Z. Wang, B. McCornac, and A.M. Beese, “Quantitative relationship between anisotropic strain to failure and grain morphology in additively manufactured Ti-6Al-4V,” *Materials Science and Engineering: A*, 706, 287–294, 2017.
- [50] N. Poondla, T. Srivatsan, A. Patnaik, and M. Petraroli, “A study of the microstructure and hardness of two titanium alloys: Commercially pure and Ti6Al4V,” *Journal of Alloys and Compounds*, 486, 162–167, 2009.
- [51] P.J. Wolcott, A. Hehr, and M.J. Dapino, “Optimized welding parameters for Al 6061 ultrasonic additive manufactured structures,” *Journal of Materials Research*, 29, (17), 2055–2065, 2014.
- [52] ThorLabs, “GRIN fiber optic collimators/couplers, single mode fiber,” Accessed at: https://www.thorlabs.com/newgrouppage9.cfm?objectgroup_id=1340, 2019.
- [53] ASTM International, “E8: Standard test methods for tension testing of metallic materials,” 2013.
- [54] Battelle Memorial Institute, “Metallic Materials Properties Development and Standardization (MMPDS),” 2012.
- [55] ASTM International, “E466-15: Standard practice for conducting force controlled constant amplitude axial fatigue tests of metallic materials,” 2015.
- [56] ASTM International, “E739-10: Standard practice for statistical analysis of linear or linearized stress-life (S-N) and strain-life (ϵ -N) fatigue data,” 2010.

- [57] ASTM International, “Statistical planning and analysis for fatigue experiments,” 2017.
- [58] ASTM International, “E647: Standard test method for measurement of fatigue crack growth rates,” 2015.
- [59] J.J. Schomer and M.J. Dapino, “High temperature characterization of fiber bragg grating sensors embedded into metallic structures through ultrasonic additive manufacturing,” *Conference on Smart Materials, Adaptive Structures and Intelligent Systems*, 1–8, 2017.
- [60] NASA Technical Standard, “Non-destructive evaluation requirements for fracture critical metallic components,” NASA-STD-5009, 2008.
- [61] X. Kong, J. Li, C. Bennett, W. Collins, and S. Laflamme, “Numerical simulation and experimental validation of a large-area capacitive strain sensor for fatigue crack monitoring,” *Measurement Science and Technology*, 27, (12), 2016.
- [62] X. Kong, J. Li, S. Laflamme, C. Bennett, and A. Matamoros, “Characterization of a soft elastomeric capacitive strain sensor for fatigue crack monitoring,” *Sensors and Smart Structures Technologies for Civil, Mechanical, and Aerospace Systems 2015*, 9435, 94353I, 2015.
- [63] C. Jingwei, N.P. Jack, J.C. Anthony, and W.D. Bruce, “Monitoring fatigue crack growth using nonlinear ultrasonic phased array imaging,” *Smart Materials and Structures*, 26, (5), 55006, 2017.
- [64] R.W. Hertzberg, R.P. Vinci, and J.L. Hertzberg, *Deformation and Fracture Mechanics of Engineering Materials*. John Wiley & Sons, 5th ed., 2013.
- [65] ASTM International, “Heat treating of aluminum alloys,” 1991.